

REPAIR OF STEEL BRIDGE GIRDERS DAMAGED BY DISTORTION-INDUCED FATIGUE
By

Daniel Nagati

Submitted to the graduate degree program in Civil Engineering and the Graduate Faculty of the
University of Kansas in partial fulfillment of the requirements for the degree of Master of
Science.

Co- Chairperson Dr. Caroline Bennett

Co- Chairperson Dr. Adolfo Matamoros

Dr. Stanley Rolfe

Dr. Ron Barrett- Gonzalez

Date Defended: 06/07/2012

The Thesis Committee for Daniel Nagati
certifies that this is the approved version of the following thesis:

REPAIR OF STEEL BRIDGE GIRDERS DAMAGED BY DISTORTION-INDUCED
FATIGUE

Co- Chairperson Dr. Caroline Bennett

Co- Chairperson Dr. Adolfo Matamoros

Dr. Stanley Rolfe

Dr. Ron Barrett- Gonzalez

Date approved: 06/07/2012

EXECUTIVE SUMMARY

Distortion-induced fatigue in steel bridge girders is a common source of damage, especially in bridges built prior to the mid-1980s. Several different retrofit measures have been developed to extend the useful life of bridges affected by distortion-induced fatigue damage, and implemented with various degrees of success to either slow or arrest the growth of fatigue cracks. Experimental and analytical simulations were conducted to determine the efficacy of several different retrofit measures for distortion-induced fatigue. A new type of repair, designated as “angles-with-back plate,” was developed based on results from computer simulations and experimental observations. The angles-with-back plate retrofit measure was developed placing emphasis on simplicity of construction, minimizing construction costs, and minimizing traffic disruptions. Computer simulations and physical tests of 9 foot girder subassemblies were carried out to evaluate the performance of the angles-with-back plate retrofit measures in terms of the reduction in stress demand at critical locations and its ability to prevent further crack propagation.

The second thrust of the study was to investigate the use of composite materials to repair fatigue damage. Assemblies with welded cover plates, a type of connection detail well known for its susceptibility to fatigue damage, were repaired using prefabricated composite overlays. This type of connection detail was chosen for the study because there is a significant body of literature on its behavior under fatigue loading and because there are well-established methods of repair that could be used as a benchmark to evaluate the performance of the composite materials. A preceding study showed that the biggest problem with this kind of retrofit measure was the tendency of composite overlays to debond from the steel due to peel stresses induced by the curvature of the assemblies when subjected to bending. Because debonding of the overlay

renders the repair ineffective, the goal of this study was to evaluate a method to prevent that from happening. The improved retrofit measure consisted of placing steel plates on top of the composite overlays. The steel plates would then be fastened to the assembly with structural bolts with the goal of maintaining the steel-overlay interface in compression. The compressive stress would preclude any cracks that develop along the steel-overlay interface from propagating, effectively preventing debonding of the overlays.

This thesis is organized in three different sections. The first, titled “Repair of Distortion-Induced Fatigue Cracks in Steel Bridge Girders” describes the analytical and experimental programs used to evaluate the angles-with-back plate retrofit measure. The second part, titled “Use of Bolted CFRP Overlays to Prevent Fatigue Damage in Welded Steel Cover Plates,” describes an analytical study to evaluate various configurations of composite overlays bolted to welded cover plates and a steel plate. The third portion of this thesis titled “Load Cells for Scale Bridge Model” details the design, fabrication, and preparation of custom-made load cells used for monitoring the load distribution in a 30-foot long reduced-scale model of a steel girder bridge test. The reduced-scale model of the bridge is intended to verify findings from research developed using component tests to make sure that those findings are applicable to complete bridge systems. Using a model of a complete bridge system allows proper simulation of the complex interactions that will take place between adjacent girders and the effect of components such as the bridge deck.

ACKNOWLEDGEMENTS

Completion of this research would not have been possible without contributions from the following people:

Special appreciation is due to Drs. Caroline Bennett, Adolfo Matamoros, Stanley Rolfe, and Ronald M. Barrett- Gonzalez, for their guidance and assistance.

I would like to thank the following state DOTs participating in Pooled Fund Study TPF-5(189): Kansas, California, Iowa, Illinois, New Jersey, New York, Oregon, Pennsylvania, Tennessee Wisconsin, and Wyoming, as well as the Federal Highway Administration for their contributions. Additionally, the assistance of the University of Kansas Transportation Research Institute (KU TRI) and its staff is greatly appreciated.

The experimental research described in this thesis was made possible by the assistance of laboratory personnel Jim Weaver and Matt Maksimowicz. Further, I would like to thank my fellow graduate students: Gary G. Simmons, Temple Richardson, Fatih Alemdar, Nathan Hickey, Say Hak Bun, Dr. Matt O'Reilly, and Amanda Hartman.

I would also like to thank my family and friends for their support and encouragement.

TABLE OF CONTENTS

Acceptance page	ii
Executive Summary	iii
Acknowledgements.....	v
Table of Contents	vi
List of Figures	viii
List of Tables	xi
List of Symbols	xii
List of Acronyms	xiii
List of Subscripts	xiii
Chapter 1 Retrofit of Distortion-Induced Fatigue Cracks in Steel Bridge Girders. 1	
Abstract	1
Introduction and background	2
Objective and scope	8
Computer simulations	9
Experimental program	24
Retrofit Measures.....	31
Experimental results.....	34
Conclusions.....	48
Chapter 2 Use of Bolted CFRP Overlays to Prevent Fatigue Damage in Welded Steel Cover Plates	50
Abstract	50
Introduction and Background	50
Objective and Scope	54
Computer Simulation and Results	54
Conclusions.....	62
Chapter 3 Load Cell Design for Scale Bridge Model	63
Abstract	63
Introduction.....	63
Objective and Scope	64
Load Cell Design	65
Computer Simulation.....	68
Fabrication, Instrumentation, and Calibration	70

Summary and Conclusions	74
References.....	76

LIST OF FIGURES

Figure 1-1: Out of plane distortion in bridge girder	3
Figure 1-2: Bottom view of simulated bridge model (Hassel 2011)	6
Figure 1-3: Deflected shape of the bridge model under truck load (Hassel 2011)	6
Figure 1-4: Deflected shape of bridge section in a region of positive moment (Hassel 2011)	7
Figure 1-5: Close-up view showing stress demand at the web-gap region of the deflected girder (Hassel 2011).....	7
Figure 1-6: Detailed view of the stress demand at the web-gap region of an external bridge girder (Hassel 2011)	8
Figure 1-7: Deformed configuration of girder specimen: a) aerial view b) center cut	9
Figure 1-8: Experiment setup.....	11
Figure 1-9: Girder specimen a) plan b) elevation c) section.....	12
Figure 1-10: Observed crack patterns superimposed on the results from the simulation models for web-gap regions of specimens 1 and 2 (observed cracks shown as white lines).	13
Figure 1-11: Pre-defined paths for sampling of stress demands in the various FE models.	14
Figure 1-12: Stress field comparison a) No retrofit b) Crack stop hole retrofit	15
Figure 1-13: Peak demand at web-gap region vs. crack length for retrofitted specimens a) HSS for stiff back plate configurations b) HSS for flexible back plate configurations, c) J-Integral for various back plate configurations.	23

Figure 1-14: a) computed stresses without retrofit b) angle retrofit configuration c)	
computed stresses with retrofit.	24
Figure 1-15: Instrumentations on 9-ft girder specimen.	27
Figure 1-16: Comparison between LVDT readings and computed deformations.....	28
Figure 1-17: Strain gage readings compared with simulation model results.....	29
Figure 1-18: Dimensions of angles and plate evaluated experimentally. a) side view, b)	
angle dimensions, c) plate dimension	32
Figure 1-19: Angle retrofit with plate a) back plate, b) angles.....	32
Figure 1-20: a) Crack stop holes in bottom web-gap region specimen 2, b) Crack	
progression at the bottom web-gap region of specimen 2, un-retrofitted, c)	
Crack stop holes at the top web-gap region	34
Figure 1-21: Experimental results for specimen 2 trials.....	36
Figure 1-22: Summary of Specimen 2 crack growth	42
Figure 1-23 Summary of Specimen 3 horizontal crack growth.....	43
Figure 1-24: Summary of Specimen 3 stiffener crack growth.....	44
Figure 1-25: Summary of Specimen 3 horizontal crack growth in the unretrofitted	
configuration	45
Figure 1-26 Summary of Specimen 3 stiffener crack growth in the unretrofitted	
configuration	46
Figure 1-27: Top LVDT displacement minima and maxima.....	47
Figure 1-28: Middle LVDT displacement minima and maxima	47
Figure 1-29: Specimen 3 strain maxima and minima	48
Figure 2-1: Welded cover plate with proposed bolted CFRP retrofit.....	52

Figure 2-2: Schematic Category E' fatigue specimen (Villhauer 2011).....	53
Figure 2-3: Schematic of Three-Point Bending Fixture with CFRP-Stiffened Specimen (Kaan 2012)	54
Figure 2-4: Welded cover plate plan and elevation	55
Figure 2-5: Rectilinear overlay model	57
Figure 2-6: Curved overlay model	57
Figure 2-7: Section cut of curved overlay showing S33 stresses.....	58
Figure 2-8: Section cut of $\frac{1}{2}$ -in. overlay showing S33 stresses	59
Figure 2-9: Section cut of overlay with closer bolt spacing showing S33 stresses	60
Figure 2-10: Section cut of specimen without a resin pool showing S33 stresses	61
Figure 2-11: Section cut of specimen with 1-in. resin pool showing S33 stresses.....	61
Figure 3-1: View of end of bridge setup with load cells in place	64
Figure 3-2: Load cell at girder support	66
Figure 3-3: Load cell schematic.....	67
Figure 3-4: Load cell schematics: a) tension base b) compression piece c) assembly	67
Figure 3-5: Computed stresses in load cell assembly	69
Figure 3-6: Computed stresses in load cell alone	69
Figure 3-7: Fabricated load cells.....	70
Figure 3-8: Strain gage diagram (Vishay 2012)	71
Figure 3-9: Load cell wiring diagram	72
Figure 3-10: Dual-grid gage after wiring.....	72
Figure 3-11: Load cell after gaging and wiring	73
Figure 3-12: Load cell calibration plot	74

LIST OF TABLES

Table 1-1: Maximum HSS for retrofitted model with 2 cracks in the bottom web-gap region. Parametric studies 1 and 2.	18
Table 1-2: Maximum HSS for retrofitted model in the bottom web-gap region. Parametric study 3.	21
Table 1-3: Tensile Coupon Tests	26
Table 1-4: Experimental Program.....	30
Table 1-5: Crack growth	40
Table 1-6: Crack length	41
Table 2-1: Stresses at composite-resin/resin-steel interfaces for configurations analyzed	62

LIST OF SYMBOLS

<u>Symbol</u>	<u>Description</u>	<u>Units (SI, US Imp.)</u>
<i>a</i>	Crack Length	[mm], [in.]
<i>d</i>	Depth	[mm], [in.]
<i>E</i>	Modulus of Elasticity	[MPa], [ksi]
<i>f</i>	Flexible	
<i>L</i>	Specimen Length	[mm], [in.]
<i>m</i>	Medium	
<i>N</i>	Fatigue Loading Cycles	
<i>s</i>	Stiff	
<i>t</i>	Thickness	[mm], [in.]
<i>x</i>	Longitudinal Distance	[mm], [in.]
Δy	Change in Deflection	[mm], [in.]
$\Delta\sigma$ or dS	Stress Range	[MPa], [ksi]
ϵ	Strain	[mm/mm], [in./in.]
σ	Stress	[MPa], [ksi]

LIST OF ACRONYMS

<u>Acronym</u>	<u>Description</u>
A	Angle
AASHTO	American Association of State Highway and Transportation Officials
BP	Back Plate
CFRP	Carbon Fiber Reinforced Polymer
CP	Connection Plate
DOT	Department of Transportation
FEA	Finite Element Analysis
HSS	Hot Spot Stress
LRFD	Load and Resistance Factor Design
LVDT	Linear Variable Differential Transformer
SIF	Stress Intensity Factor
UIT	Ultrasonic Impact Treatment
XFEM	Extended Finite Element Method

LIST OF SUBSCRIPTS

c	Critical
max	Maximum
s	Steel

CHAPTER 1 RETROFIT OF DISTORTION-INDUCED FATIGUE CRACKS IN STEEL BRIDGE GIRDERS

Abstract

Several studies have identified distortion-induced fatigue as the leading cause of cracks in steel bridges built prior to the mid-1980s (Lindberg and Schultz 2007, Roddis 2001). Experimental and computer simulations of 914-mm (36-in.) deep girder-cross frame subassemblies subjected to cyclic loading were carried out to study the effects of distortion-induced fatigue and to evaluate the effectiveness of various retrofit measures. Previous repair methods for distortion-induced fatigue damage have attempted to reduce the stress demand at the critical web-gap region by increasing the flexibility of the girder web in the out-of-plane direction or by restraining the lateral motion of the web by fixing the connection stiffener to the girder flange. A new approach was investigated in this study intended to reduce the stress demand in the web-gap region by re-distributing the out-of-plane force transferred through the girder-cross frame connection over a larger area of the girder web.

A new retrofit measure is proposed based on this approach, which consists of adding steel angles connecting the girder web and the connection plate (CP), and a steel plate on the back side of the girder web to distribute the lateral force over a wider region of the web. Experimental and computer simulation results are presented showing that this repair method is very effective in preventing the growth of horseshoe-shaped cracks around the web cross-frame connection and of horizontal cracks near the junction between the flange and web.

Introduction and Background

Fatigue cracks in steel girders are frequently found during inspections of older bridge structures (Lindberg and Schultz 2007). These cracks generally initiate in areas of a bridge affected by large stress demands induced by geometric discontinuities. A national survey on the types of fatigue cracks observed in steel bridges was performed as part of a study on distortion-induced fatigue sponsored by the Minnesota Department of Transportation (Mn/DOT) (Lindberg and Schultz 2007). In response to the survey, DOT engineers from various states reported 11 different types of commonly observed fatigue cracks. One of the most frequently reported areas exhibiting fatigue damage were transverse stiffener web-gaps in positive and negative moment regions of girders (Keating 1994). This is consistent with a study by Roddis and Zhao (2001) which states that out-of-plane distortion was one of the main reasons for fatigue cracks in bridges nationwide. Roddis and Zhao (2001) also stated that the positive moment region was more vulnerable to fatigue cracks than the negative moment region. Deformations induced by out-of-plane distortion are illustrated in Figure 1-1. When adjacent girders experience different vertical deflections due to passing traffic, transverse stiffeners can cause out-of-plane distortion on the girder web. Out-of-plane distortion of the web-gap region and the high localized deformations caused by it induce large stress demands in the web and the connection welds, which can significantly decrease the fatigue life of bridges (Jajich and Schultz 2003).

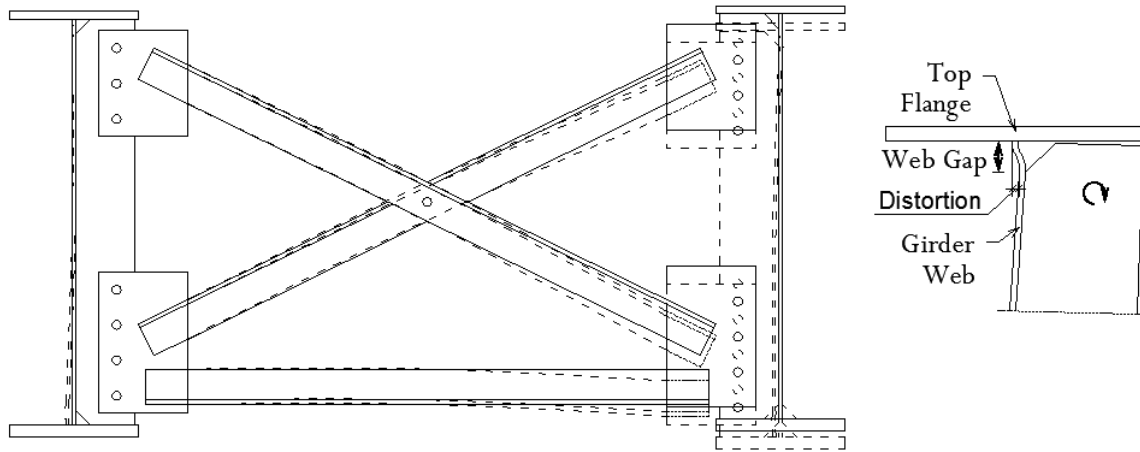


Figure 1-1: Out of plane distortion in bridge girder

A web-gap region is created when a connection plate is clipped at the top or bottom, leaving a gap between the edge of the connection plate and the unconnected girder flange (Fig. 1-1). This type of connection detail was widely used in the United States before the mid-1980s. The connection detail was implemented in this manner because it is very difficult to achieve a good quality weld at the intersection of the web and flange (Castiglioni et al. 1988), and because there were concerns that welding the connection plate to the tension flange would lead to fatigue damage, a problem that was observed in European bridges early in the last century (Roddis and Zhao 2001). Roddis and Zhao (2001) indicate that it was common practice not to weld connection plates to the compression flange also to avoid the introduction of AASHTO fatigue category E connection details.

Retrofit measures for distortion-induced fatigue documented in the literature attempt to reduce the high localized stress demand in the web-gap region by two different approaches: some repairs attempt to reduce the stress demand by making the plate-to-web connection more flexible, while others introduce an alternate load path by adding a very stiff connection between the connection plate and the flange. The flexibility of the web-gap region can be increased

through several alternatives, including the introduction of a slot at the edge of the connection plate, cropping the stiffener, and removing diaphragms. Adding connectivity, which increases the stiffness of the connection, is commonly implemented by welding or bolting angles to the flange. Performing this type of repair often requires removal of the concrete deck (Keating and Fisher 1987; Fisher 1990; Cousins and Stallings 1998) to access the top flange. The drilling of crack-stop holes is the most commonly applied retrofit measure discussed in the literature, and can be used in combination with the retrofits measures listed previously.

The research presented in this thesis investigates two repair methods for cracks observed in web-gap regions of bridges with distortion-induced fatigue damage. These cracks were repaired using a simple reinforcement scheme applied at the web-gap region consisting of two angles and a back plate. The drilling of crack-stop holes at the tips of the fatigue cracks, a simple repair technique often used in steel bridges was also evaluated.

Research about the repair of distortion-induced fatigue cracks in web-gap regions of steel girders consisted of experimental and computer simulations of 9-ft-long girder segments. The girder segments were subjected to cyclic loading applied through a cross-frame that caused distortion of the web-gap region. Computer simulations consisted of linear analyses of high-resolution Finite Element (FE) models of the girder specimen. Calculated stress demands and potential crack propagation patterns obtained from the FE simulations were found to be in excellent agreement with direct observations from the physical simulations of the specimens. Locations of maximum principal tensile stress computed with the FE models were found to be very good indicators of the propagation path followed by fatigue cracks in the girder subassemblies.

Comparison between the behavior of test subassembly and a bridge structure

Given the interactions that exist between primary and secondary actions in a bridge, a complete bridge system provides a far superior means to evaluate the efficacy of retrofit measures than subassemblies. The main advantage of subassemblies is that testing can be performed at a significantly lower cost, allowing multiple simulations at a fraction of the cost of a single simulation of a bridge system. Because the former technique was employed in this study, a comparison was carried out between results from high-resolution computer simulations of subassemblies and complete bridge systems. A large-scale analytical study on distortion-induced fatigue in steel bridges, comprising more than 1000 high-resolution simulations of bridge systems with similar girder dimensions as those used in the subassemblies evaluated in this study, was carried out by Hassel (2011). FE simulation results, illustrated in Figs. 1-2 through 1-6, show that the distribution of stresses in the web-gap region of the subassemblies was similar to that found in the web-gap region of the two-span continuous model bridge employed by Hassel. In both instances the main areas of vulnerability were at the weld between the connection plate and the girder web, and at the weld between the web and the flange (Figs. 1-5 and 1-6).

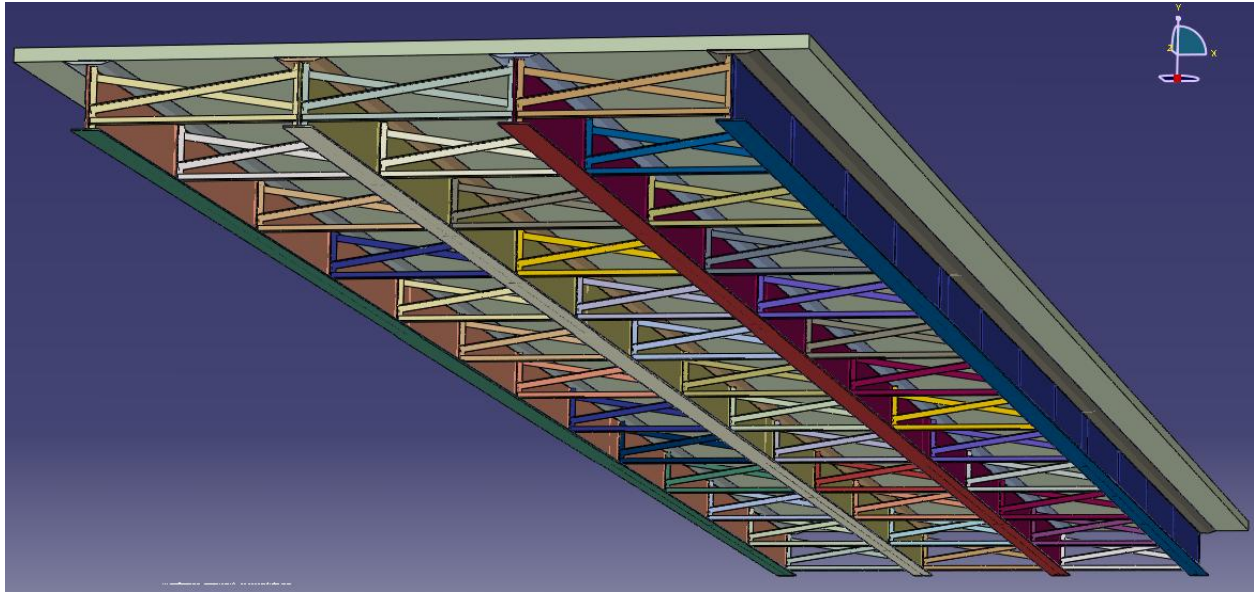


Figure 1-2: Bottom view of simulated bridge model (Hassel 2011)

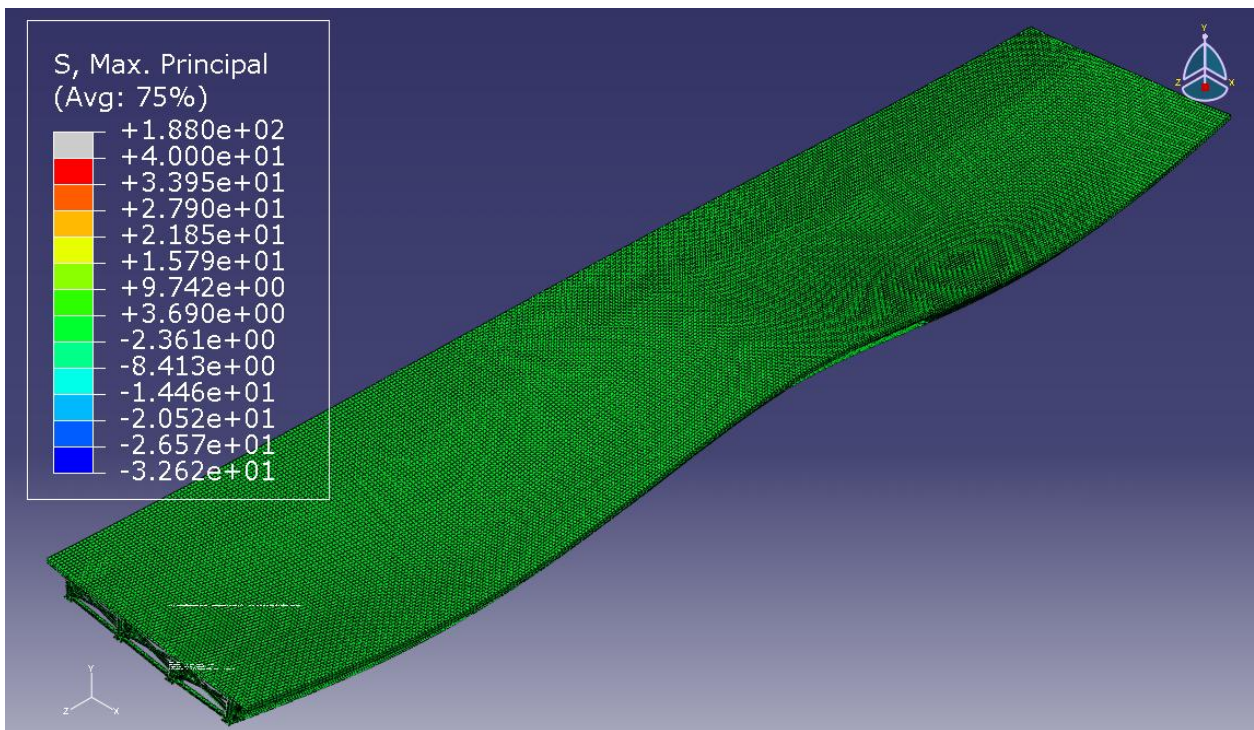


Figure 1-3: Deflected shape of the bridge model under truck load (Hassel 2011)

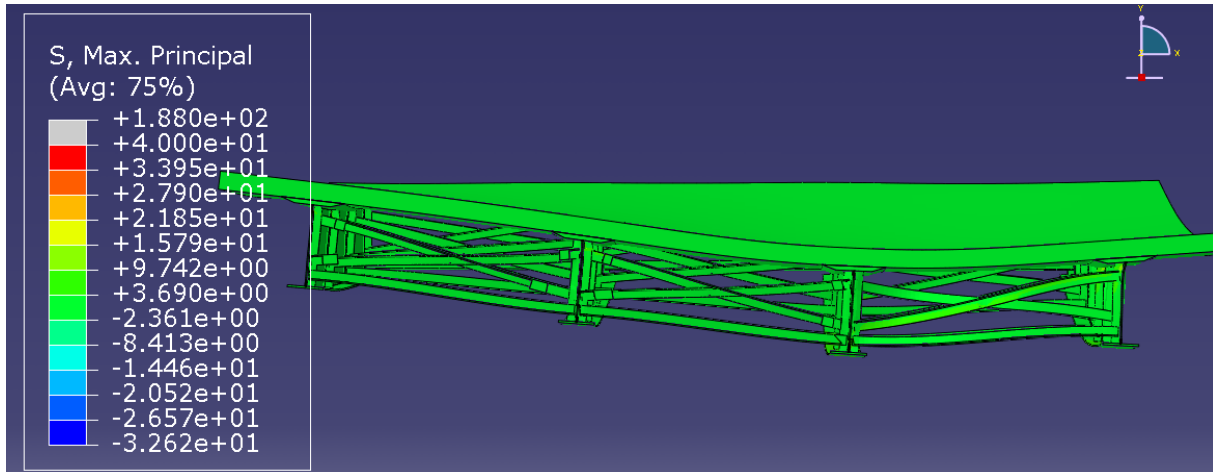


Figure 1-4: Deflected shape of bridge section in a region of positive moment (Hassel 2011)

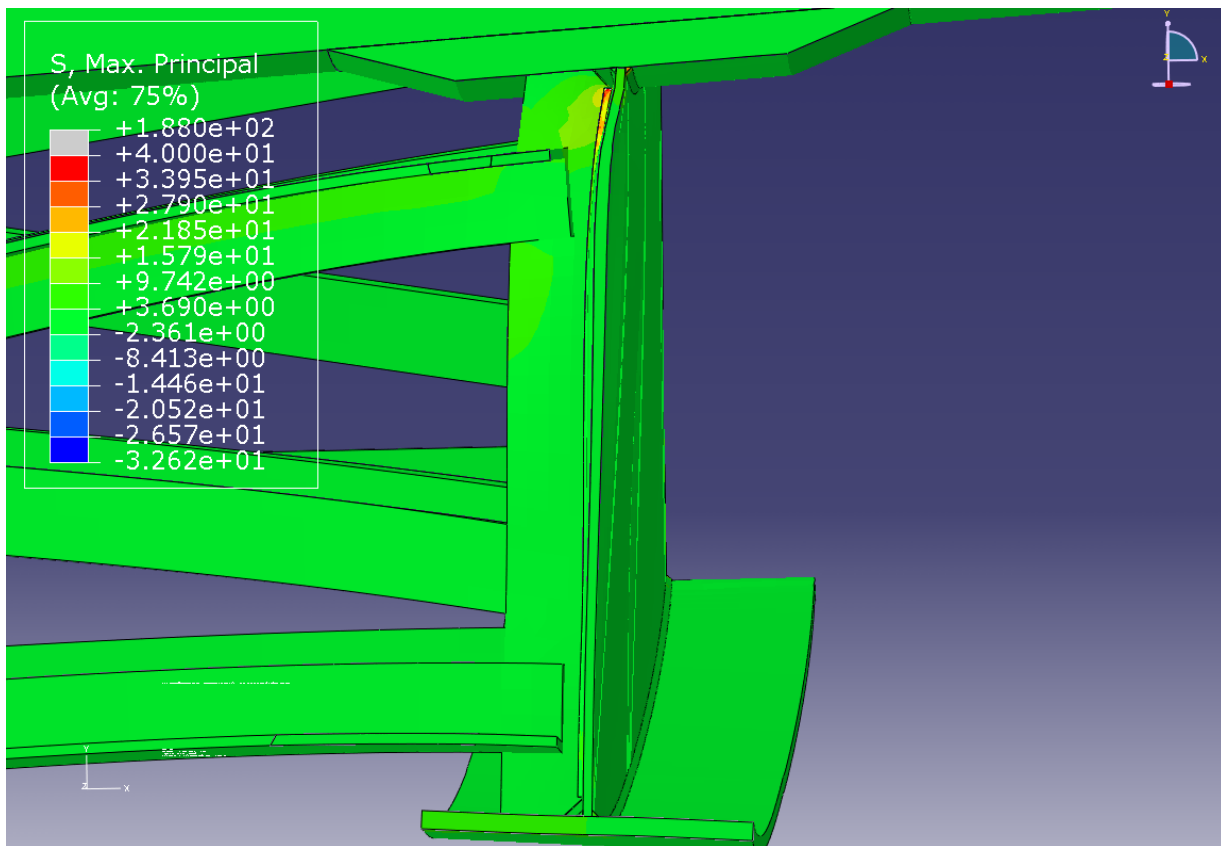


Figure 1-5: Close-up view showing stress demand at the web-gap region of the deflected girder (Hassel 2011)

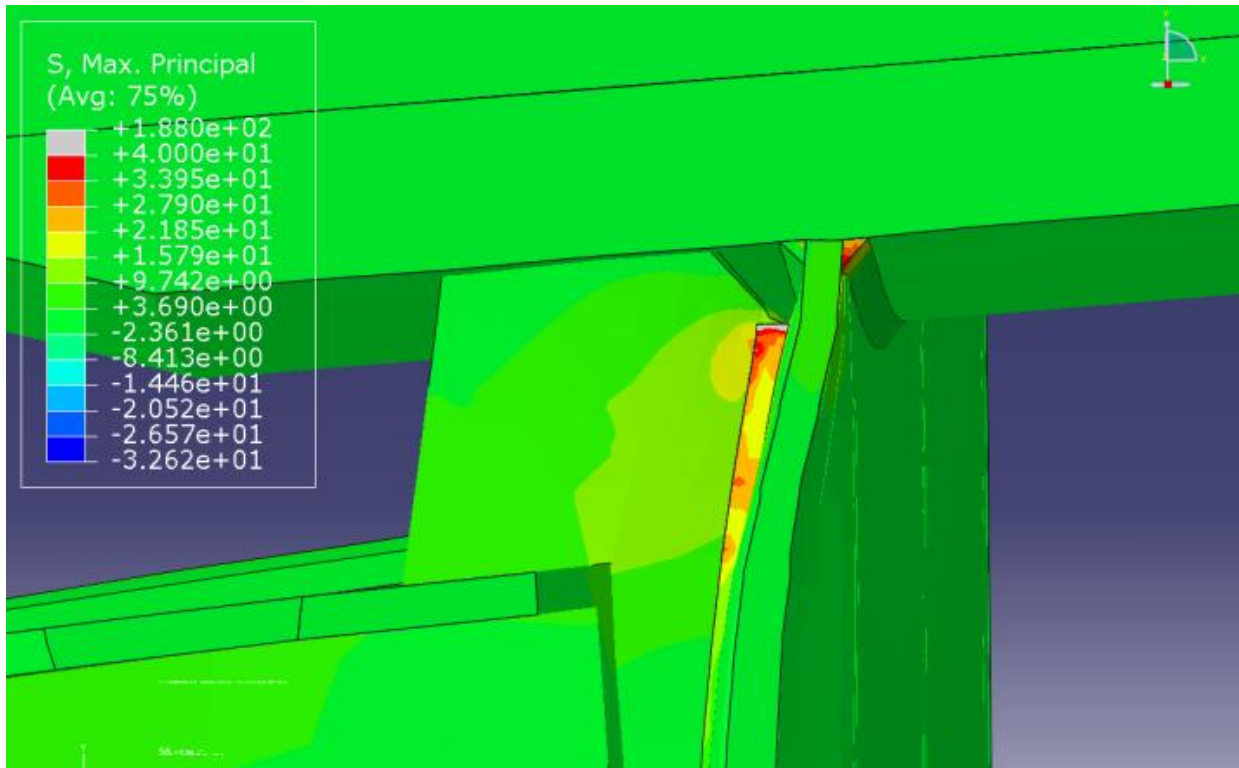


Figure 1-6: Detailed view of the stress demand at the web-gap region of an external bridge girder

(Hassel 2011)

Objective and Scope

The main objective of this study was to investigate repair methods for distortion-induced fatigue cracks in the web-gap region of bridge girders. The study included a suite of Finite Element (FE) analyses to investigate the effect of various retrofit measures and crack geometries on the stress distribution in the web-gap region. The performance of two repair methods was investigated experimentally: 1) drilling of crack-stop holes and 2) providing connectivity by attaching angles to the connection plate and the girder web, and bolting the angles to a steel bar on the opposing side of the girder web (referred to as angles-with-back plate repair).

Computer Simulations

The computer models were created to resemble as closely as possible the girder-cross frame subassemblies that were tested (Fig. 1-7). Computer simulations of a full bridge with similar girder dimensions carried out for a different study (Hassel 2011) showed good agreement between the stress fields computed at the web-gap region of the model bridge and those computed for the specimens evaluated in this study. The dimensions of the specimens and the measured material properties are described in the experimental program section. Linear-elastic FE models were created using 8-node brick elements, each with 24 degrees of freedom. The number of elements ranged from 1 to 2 million, depending on the retrofit measure that was modeled. An 813-mm (32-in.) wide strip with a reduced mesh size was defined in the girder web, centered on the cross-frame connection plate, spanning from the bottom to the top flange. The size of the elements in this strip was set as 3-mm (0.10-in) to improve the accuracy of the calculated stress field in this region. A 76-mm (3-in.) wide vertical strip of tetrahedral elements was used to transition from the fine mesh to a 10-mm (0.38-in.) coarser mesh used to model the web of the girder in locations away from the cross frame.

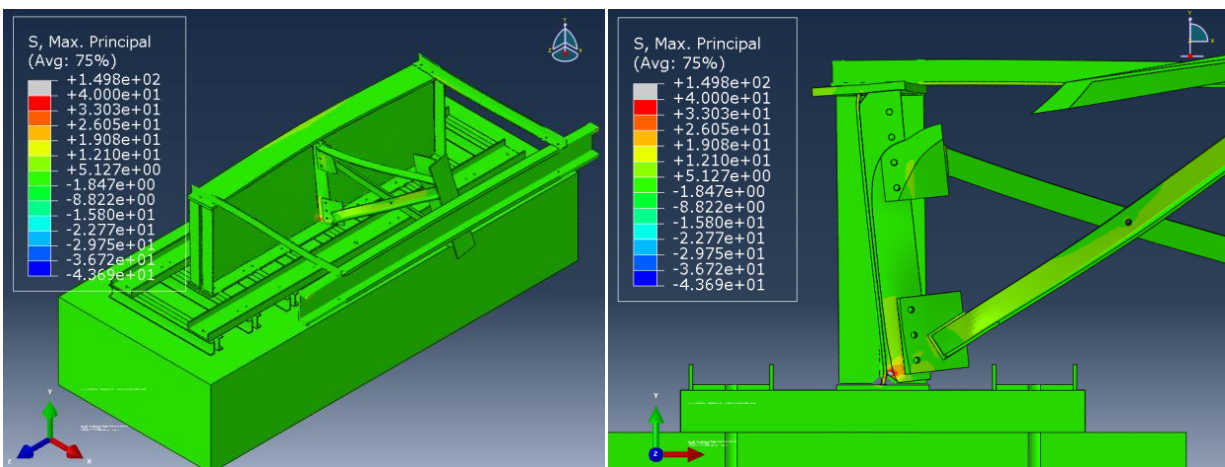


Figure 1-7: Deformed configuration of girder specimen: a) aerial view b) center cut

The connection plate was partitioned to allow for varying element types and mesh sizes around the bolt holes and the 32-mm (1-¹/₄-in.) clipped ends. A swept hexagonal mesh with 5-mm (0.2-in.) elements was used around the bolt holes, and tetrahedral elements were used in the clipped ends. Everywhere else in the connection plate, 5-mm (0.2-in.) hexagonal elements were used. A similar meshing technique was used to model the end stiffeners. The hexagonal element size used away from the clipped edges was 8-mm (0.3-in.).

All four web-to flange fillet welds, which were 5-mm (³/₁₆-in.) in size, were modeled with a triangular cross section using structured hexagonal elements. All five web-to-connection plate fillet welds were also modeled with a triangular cross section but in this case using tetrahedral elements. The fillet welds were placed all around the connection plate, including the top and the bottom. All welds had a maximum element size of 3-mm (0.1-in.). The modulus of elasticity of the A36 grade steel members was defined as 200 GPa (29,000 ksi) and Poisson's ratio was defined as 0.3.

In the physical model, the steel girder was connected to the reaction floor of the laboratory through a series of channels so that the flange would be restrained from out-of-plane motion in the same manner that the axial stiffness of the concrete deck would restrict the out-of-plane motion of a bridge girder. The concrete floor was simulated in the computer model as an elastic material with a modulus of elasticity of 27,780 MPa (4,000 ksi) and Poisson's ratio equal to 0.2. The concrete mesh consisted of 102-mm (4-in.) brick elements with 16 nodes. Analyses of the subassembly were performed using models in which tensioned bolts were simulated explicitly and also with models in which the bolt force was neglected and the bolts were connected to the steel members with tie constraints. It was found that the computed stress fields at the web-gap region were very similar, with the latter type of model requiring a much lower

computational cost. For the same reason, connections between the channels and the bottom flange of the girder were simulated using tie constraints.

The computer model was loaded with a single 22,240-N (5-kip) force, applied to a WT section that was used to connect the cross braces to the actuator in the physical model (Fig. 1-8). In the computer model, the bottom of the concrete block below the specimen was modeled as fully fixed, and so were both ends of a channel connecting the two end angles to the reaction frame in the physical model (Fig. 1-8). In the computer model, the WT section where the actuator force was applied was restrained from moving along the direction parallel to the longitudinal axis of the girder. Figures 1-8 and 1-9 show the girder specimen and the experimental setup.



Figure 1-8: Experiment setup.

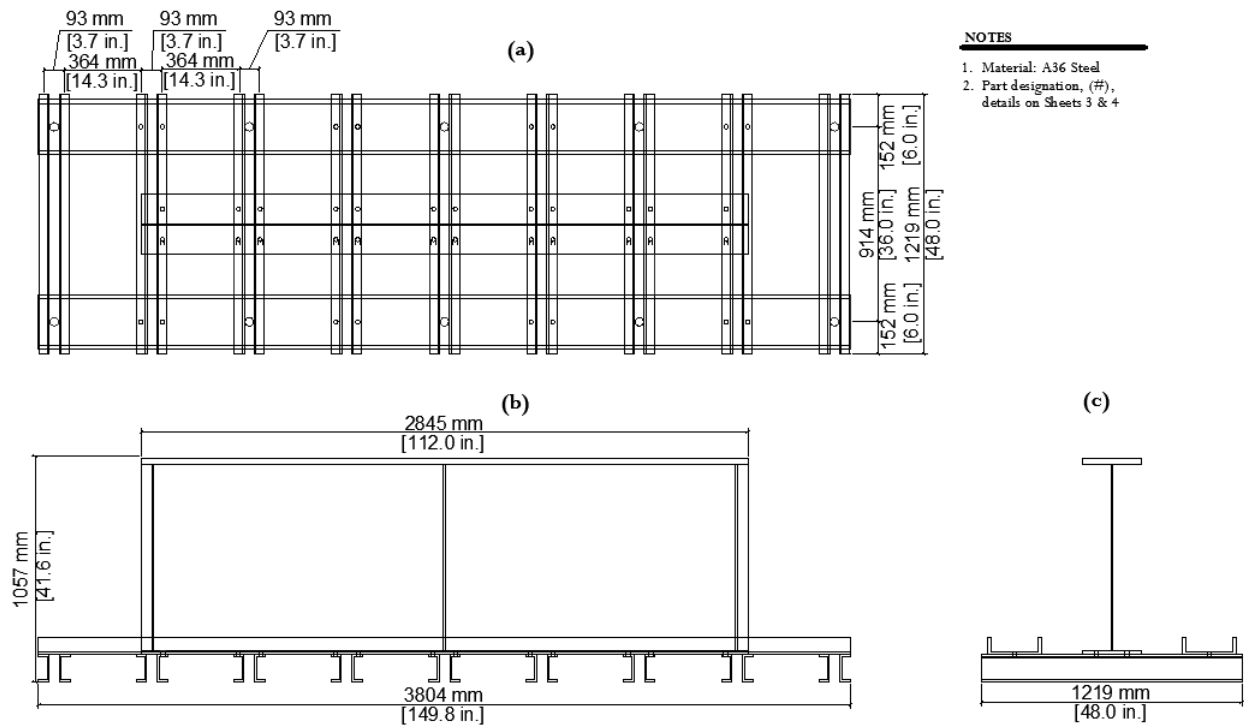


Figure 1-9: Girder specimen a) plan b) elevation c) section

Computed stresses from models with different retrofit measures were compared using the hot spot stress (HSS) technique. The HSS technique was adopted to obtain a more reliable measure of demand in areas of the web-gap region where there were large stress gradients, such as near welded or bearing connections. Maximum principal stresses were used as a measure of vulnerability to fatigue damage because areas with the largest maximum principal stress demands in the model correlated well with locations where cracks formed in the specimens (Fig. 1-10).

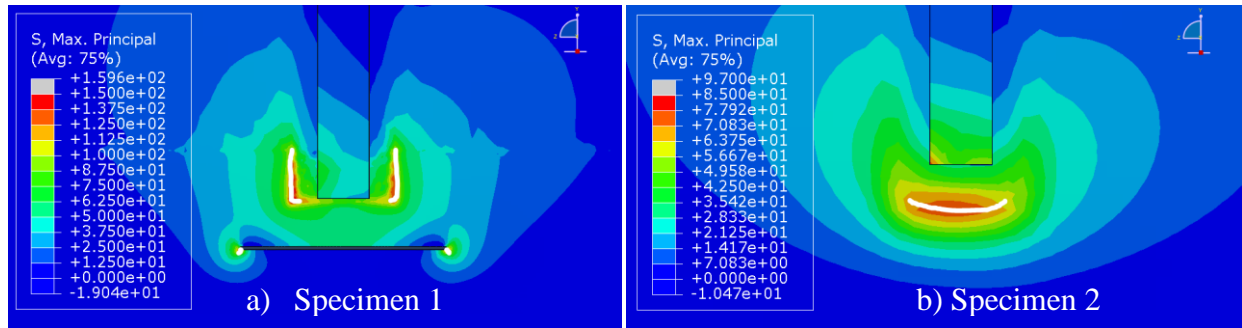


Figure 1-10: Observed crack patterns superimposed on the results from the simulation models for web-gap regions of specimens 1 and 2 (observed cracks shown as white lines).

In accordance with the definition of HSS used in this study, paths for sampling the stresses were defined at a distance of 5-mm ($3/16$ -in.) away from the weld, equivalent to half the thickness of the web (10-mm, $3/8$ -in.) (Fig. 1-11). HSS sampling paths were defined only near locations where cracks were observed in the specimens. HSS Path #1 Bottom was defined as a horseshoe-shaped path in the bottom web-gap of the subassembly. HSS Path #2 Bottom was defined as a horizontal path above the crack that formed in the web-to-flange weld in the bottom web-gap of the subassembly. Similar paths were defined and sampled in the top web-gap of the subassembly when cracks were observed in the experiment. The J-Integral and stress intensity factors (SIF) at the tip of simulated cracks were computed as a measure of propensity for crack growth. A total of 5 contours were evaluated in the calculations, at points evenly spaced through the thickness of the web.

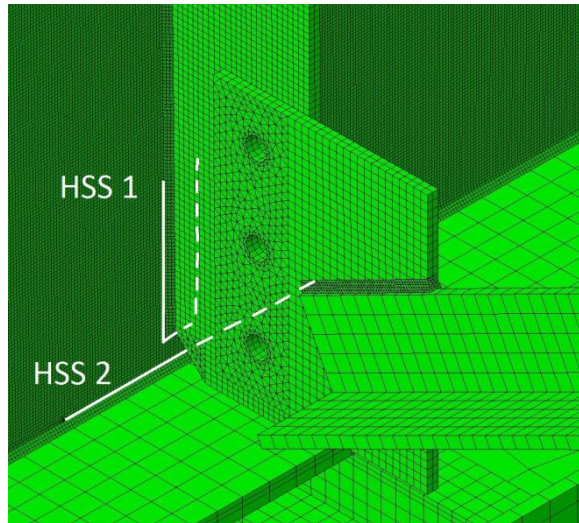


Figure 1-11: Pre-defined paths for sampling of stress demands in the various FE models.

Crack stop holes

During the physical simulation of the 9-ft subassemblies, cyclic loads were applied while crack growth caused by the distortion of the web-gap was monitored. In one of the latter test trials, crack-stop holes with a diameter of 19-mm ($3/4$ -in.) were drilled at the tip of the cracks, at the locations shown in Fig. 1-20. Crack-stop holes were placed in the FE models in the same top and bottom web-gap locations that were drilled in the specimen to evaluate their effect on the stress field. Four of the holes shown in Fig. 1-12b were used to attach angles to the web and were not intended to be crack-stop holes. Figure 1-12 shows the computed stress fields with and without crack-stop holes. The comparison shows that the stress demands were virtually the same.

The two HSS sampling paths in the model with crack stop holes were defined at a distance of half the thickness of the web away from the web-to-connection plate weld. Simulations were performed to establish a comparison between an unretrofitted model with two cracks in the bottom web-gap region and a model with the same crack pattern but with crack-stop holes (Fig.

1-12). The maximum HSS value at Path #1 decreased by 27% with the drilling of the crack stop holes, while the maximum HSS along Path #2 decreased by 16%. The stress fields presented in Fig. 1-12 show that the drilling of crack-stop holes did not significantly reduce the stress demand, and that the reduction was not likely sufficient to prevent the existing cracks from propagating.

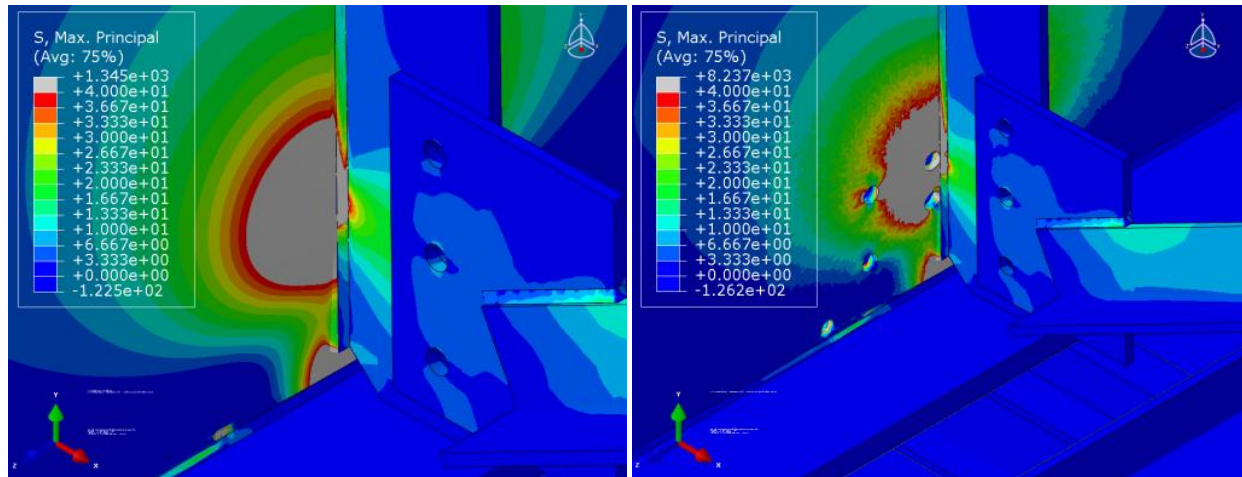


Figure 1-12: Stress field comparison a) No retrofit b) Crack stop hole retrofit

Angles-with-plate repair

This repair was developed based on experimental observations from simple three-point bending specimens with welded connections repaired with composite overlays. Test results showed that providing an alternate load path around the weld was a highly effective method to reduce the stress demand at the weld and led to a negligible rate of crack growth (Alemdar et al. 2011). Although the shape of the three-point bending specimens was different, there was a strong similarity with the web-gap region because computer and experimental simulations showed that horseshoe-shaped cracks in the latter type of connection originate near the connection plate-to-web weld. Computer simulations in which the web-gap region was repaired with composite materials were evaluated as part of this study, and this method proved to be

highly effective. A simpler solution in terms of fabrication and installation in the field, which constitutes the focus of this study, was developed by using steel angles instead of composite blocks to reduce the stress demand at the welded connection.

The configuration of this retrofit measure is shown in Fig. 1-14b, Fig. 1-18 and Fig. 1-19. Parametric analyses of the angles-with-plate retrofit measure were performed to determine the optimal back plate and angle dimensions. The first parametric study involved varying the angle and back plate thicknesses, while the other dimensions were kept constant. The crack pattern in the model was the same used to evaluate the performance of the crack-stop hole retrofit, with a 102-mm (4-in.) long horseshoe crack and a 203-mm (8-in.) long horizontal crack in the bottom web-gap of the subassembly. The horseshoe-shaped crack followed the toe of the CP-to-web fillet weld, while the horizontal crack was placed along the web-to-bottom flange weld. The back cover plate and angle thicknesses evaluated were 6-mm ($\frac{1}{4}$ -in.), 13-mm ($\frac{1}{2}$ -in.), and 25-mm (1-in.). Computed stress demands are summarized in Table 1-1. All values in Table 1-1 correspond to reductions in the calculated elastic stress demand with respect to the unretrofitted configuration and ranged between 93 and 98%, which clearly shows that this retrofit measure, regardless of configuration, significantly reduced the computed stress demand in the bottom web-gap region. Although variations in the stress demands were found to be small, some trends that are helpful in choosing an optimum configuration for the retrofit measure could be discerned.

The stress demands in Table 1-1 show that for all back plate configurations, increasing the thickness of the angles led to a reduction in the peak stress demand at the path near the horseshoe-shaped crack. Increasing the stiffness of the back plate also led to a reduction in the peak stress at the path near the horseshoe-shaped crack. The effect of element stiffness on the

peak stress demand at the path near the horizontal crack was the opposite. Increasing back plate and angle stiffness led to increases in stress demand, with the exception of the configuration with the most flexible back plate, for which the stress demands were comparable for the stiff and flexible angle configurations. When the peak demand at the two paths is averaged, the configurations with the lowest stress demands were those with the thickest back plate (42 MPa, 6 ksi), with the lowest among those being the configuration with the thickest angles.

Configurations with the highest average stress demand were those with the thinnest back plate (52 MPa, 7 ksi), with the highest among those being the configuration with the thinnest plate and the thinnest angles (62 MPa, 9 ksi). These results suggest that because the stiffness of the retrofit elements (angles and back plate) had a greater effect on the stress demand near the horseshoe-shaped crack than on the stress near the horizontal crack, stiffer configurations were most effective. However, it is noted that stiffer configurations resulted in slightly higher stress demands at the path near the horizontal crack. While stress demands near the horseshoe-shaped crack were inversely proportional to the stiffness of the retrofit elements, the relationship was much more complex for the case of the horizontal crack. In general, configurations with intermediate back plates had lower stress demands, with the lowest demand corresponding to a combination of intermediate angle and thinnest back plate.

In general, the parametric study showed that increasing the stiffness of the retrofit elements reduced the fraction of the connection force being transmitted through the connection plate-to-web fillet weld, which caused an increase in the stress demand at the web-to-flange weld. More flexible retrofit elements made the retrofit measure less effective for the crack at the CP-to-web and more effective for the crack at the web-to-flange weld. It is important to emphasize that although the stiffness of the angles and the plate did have an effect on the

calculated stress demand, this effect was relatively small, and in all instances the calculated stress demands were much lower than the values computed for the unretrofitted configuration.

Table 1-1: Maximum HSS for retrofitted model with 2 cracks in the bottom web-gap region.

Parametric studies 1 and 2.

Designation	Plate Length, mm (in)	Plate Thickness, mm (in)	Angle Thickness, mm (in)	HSS Path #1 Bottom, MPa (ksi)	HSS Path #2 Bottom, MPa (ksi)
<i>sA-sBP18</i>	457 (18)	25 (1)	25 (1)	23 (3.4)	58 (8.3)
<i>mA-sBP18</i>	457 (18)	25 (1)	13 (¹ / ₂)	30 (4.3)	55 (8.0)
<i>fA-sBP18</i>	457 (18)	25 (1)	6 (¹ / ₄)	30 (4.4)	54 (7.9)
<i>sA-mBP18</i>	457 (18)	13 (¹ / ₂)	25 (1)	39 (5.6)	55 (7.9)
<i>mA-mBP18</i>	457 (18)	13 (¹ / ₂)	13 (¹ / ₂)	60 (8.6)	45 (6.5)
<i>fA-mBP18</i>	457 (18)	13 (¹ / ₂)	6 (¹ / ₄)	51 (7.4)	47 (6.9)
<i>sA-fBP18</i>	457 (18)	6 (¹ / ₄)	25 (1)	41 (5.9)	52 (7.6)
<i>mA-fBP18</i>	457 (18)	6 (¹ / ₄)	13 (¹ / ₂)	51 (7.3)	43 (6.2)
<i>fA-fBP18</i>	457 (18)	6 (¹ / ₄)	6 (¹ / ₄)	68 (9.8)	55 (8.0)
<i>mA-mBP12</i>	305 (12)	13 (¹ / ₂)	13 (¹ / ₂)	59 (8.5)	49 (7.1)
<i>mA-mBP18</i>	457 (18)	13 (¹ / ₂)	13 (¹ / ₂)	60 (8.6)	45 (6.5)
<i>mA-mBP24</i>	610 (24)	13 (¹ / ₂)	13 (¹ / ₂)	56 (8.2)	74 (10.7)
<i>mA-mBP36</i>	914 (36)	13 (¹ / ₂)	13 (¹ / ₂)	45 (6.5)	77 (11.2)

A second parametric study was performed in which the angle and back plate thicknesses were kept constant at 13-mm (¹/₂-in.), while the length of the back plate was changed. The length of the back plate was set to 305, 457, 610, and 914-mm (12, 18, 24, and 36-in.). The results are also summarized in Table 1-1. Again the results were contradictory in terms of the effect of the retrofit measure on the stress demand near the two cracks. While increasing the length of the back plate had the effect of reducing the peak stress demand near the CP-to-web weld, it increased the peak stress demand at the web-to-flange weld. Of the two critical locations, the length of the back plate had the largest effect on the stress demand near the web-to-

flange weld. If the average peak stress is used as a measure of demand, configurations with 305 and 457-mm (12 and 18-in.) plate lengths had the lowest demands, with very similar averages of 54 MPa and 53 MPa (8 and 7 ksi), respectively.

A third parametric study was conducted to evaluate the effect of crack length on the likelihood of fatigue damage for the angles-with-plate retrofit measure. Hot spot stress (HSS) values were extracted from analyses of models with varying lengths of the horseshoe-shaped and horizontal cracks. Configurations evaluated had horseshoe-shaped and horizontal crack lengths of $\frac{1}{2}$ and $\frac{1}{2}$ -in., 1 and 1-in., and 4 and 8-in., respectively. The last crack configuration, with lengths of 4 and 8-in., corresponded to the observed crack configuration at the end of the first trial for specimen 2 (Table 1-2, Fig. 1-20a), and was the same crack configuration used in the first and second parametric studies. All models had the angles-with-plate retrofit measure implemented with angle and cover plate thicknesses of 6-mm ($\frac{1}{4}$ -in.), 13-mm ($\frac{1}{2}$ -in.), and 25-mm (1-in.) evaluated for each crack configuration. In all the models of the third parametric study the length of the back plate was 457-mm (18-in.). Companion models with the angle-with-plates retrofit measure but without cracks were also analyzed to provide a basis for comparison.

The peak HSS exhibited different trends with respect to crack length along Path #1 (horseshoe-shaped crack) than it did along Path #2 (horizontal crack). For HSS Path #1 (horseshoe-shaped crack) configurations with the thickest angles and/or back plate (stiff configurations, Fig. 1-13a) the maximum stress demand corresponded to the retrofitted specimen without cracks (shown in the graphs in Fig. 1-13 as zero length). The peak HSS decreased with increasing crack length, stabilizing at approximately 75% of the peak demand computed with the unretrofitted model. The crack length at which the peak stress demand stabilized was lowest for the model with the stiffest angles. For the configuration with the thinnest angles (flexible

configuration, Fig 1-13b) and back plate the HSS values decreased with crack length for very short lengths, approximately less than 12-mm ($\frac{1}{2}$ -in.). For crack lengths longer than 12-mm ($\frac{1}{2}$ -in.), the peak stress demand increased with crack length for the configurations with the two thinnest angles. These results showed that the best alternative to reduce the stress demand near the horseshoe-shaped crack was to use the stiffest angle and back plate combination, and that the effectiveness of the retrofit measure was nearly independent of crack length.

Table 1-2: Maximum HSS for retrofitted model in the bottom web-gap region. Parametric study 3.

Designation	Plate Thickness, mm (in.)	Angle Thickness, mm (in.)	HSS Path #1 MPa (ksi)		HSS Path #2 MPa (ksi)		
<i>sA-sBP18</i>	25.4 (1)	25.4 (1)	60.0 (8.7)		102.0 (14.8)		No Cracks
<i>mA-sBP18</i>	25.4 (1)	12.7 (1/2)	65.0	9.4	103.9	15.1	
<i>fA-sBP18</i>	25.4 (1)	6.35 (1/4)	67.8	9.8	103.0	14.9	
<i>sA-mBP18</i>	12.7 (1/2)	25.4 (1)	73.1	10.6	106.2	15.4	
<i>mA-mBP18</i>	12.7 (1/2)	12.7 (1/2)	86.2	12.5	111.1	16.1	
<i>fA-mBP18</i>	12.7 (1/2)	6.35 (1/4)	95.5	13.9	110.5	16.0	
<i>sA-fBP18</i>	6.35 (1/4)	25.4 (1)	81.7	11.8	107.4	15.6	
<i>mA-fBP18</i>	6.35 (1/4)	12.7 (1/2)	99.7	14.5	114.4	16.6	
<i>fA-fBP18</i>	6.35 (1/4)	6.35 (1/4)	115.8	16.8	127.0	18.4	
<i>sA-sBP18</i>	25.4 (1)	25.4 (1)	48.7	7.1	115.0	16.7	0.5-in. horseshoe crack 0.5-in. horizontal crack
<i>mA-sBP18</i>	25.4 (1)	12.7 (1/2)	54.5	7.9	117.6	17.1	
<i>fA-sBP18</i>	25.4 (1)	6.35 (1/4)	66.7	9.7	116.8	16.9	
<i>sA-mBP18</i>	12.7 (1/2)	25.4 (1)	58.0	8.4	116.5	16.9	
<i>mA-mBP18</i>	12.7 (1/2)	12.7 (1/2)	68.8	10.0	123.6	17.9	
<i>fA-mBP18</i>	12.7 (1/2)	6.35 (1/4)	94.6	13.7	124.4	18.0	
<i>sA-fBP18</i>	6.35 (1/4)	25.4 (1)	60.2	8.7	115.6	16.8	
<i>mA-fBP18</i>	6.35 (1/4)	12.7 (1/2)	72.2	10.5	125.6	18.2	
<i>fA-fBP18</i>	6.35 (1/4)	6.35 (1/4)	94.2	13.7	138.1	20.0	
<i>sA-sBP18</i>	25.4 (1)	25.4 (1)	42.8	6.2	127.2	18.5	1.0-in. horseshoe crack 1.0-in. horizontal crack
<i>mA-sBP18</i>	25.4 (1)	12.7 (1/2)	48.8	7.1	129.5	18.8	
<i>fA-sBP18</i>	25.4 (1)	6.35 (1/4)	59.1	8.6	127.5	18.5	
<i>sA-mBP18</i>	12.7 (1/2)	25.4 (1)	53.1	7.7	128.5	18.6	
<i>mA-mBP18</i>	12.7 (1/2)	12.7 (1/2)	67.0	9.7	135.0	19.6	
<i>fA-mBP18</i>	12.7 (1/2)	6.35 (1/4)	82.6	12.0	133.4	19.3	
<i>sA-fBP18</i>	6.35 (1/4)	25.4 (1)	57.8	8.4	126.4	18.3	
<i>mA-fBP18</i>	6.35 (1/4)	12.7 (1/2)	71.1	10.3	134.9	19.6	
<i>fA-fBP18</i>	6.35 (1/4)	6.35 (1/4)	91.4	13.3	137.7	20.0	
<i>sA-sBP18</i>	25.4 (1)	25.4 (1)	38.0	5.5	60.7	8.8	4.0-in. horseshoe crack 8.0-in. horizontal crack
<i>mA-sBP18</i>	25.4 (1)	12.7 (1/2)	48.3	7.0	54.2	7.9	
<i>fA-sBP18</i>	25.4 (1)	6.35 (1/4)	49.2	7.1	52.2	7.6	
<i>sA-mBP18</i>	12.7 (1/2)	25.4 (1)	56.4	8.2	53.5	7.8	
<i>mA-mBP18</i>	12.7 (1/2)	12.7 (1/2)	76.1	11.0	64.4	9.3	
<i>fA-mBP18</i>	12.7 (1/2)	6.35 (1/4)	96.6	14.0	91.0	13.2	
<i>sA-fBP18</i>	6.35 (1/4)	25.4 (1)	53.7	7.8	50.2	7.3	
<i>mA-fBP18</i>	6.35 (1/4)	12.7 (1/2)	77.2	11.2	69.5	10.1	
<i>fA-fBP18</i>	6.35 (1/4)	6.35 (1/4)	119.7	17.4	109.2	15.8	

For HSS Path #2 (horizontal crack near the web-to-flange weld), all combinations of angle and plate thicknesses followed a trend different from that observed for HSS Path #1. For short crack lengths, between 0 and 25-mm (1-in.), the peak stress demand increased with crack length. For crack lengths larger than that, peak HSS values decreased with increasing crack length, with the magnitude of the decaying slope being a function of the stiffness of the retrofit components. For retrofit configurations with the thickest back plate or the thickest angle (Fig. 1-13a), the reduction in stress demand with respect to crack length was nearly the same regardless of the stiffness of the other retrofit component. For retrofit configurations with the thinnest back plate or angle (Fig. 1-13b) the effect of the stiffness of the other retrofit component was very significant. The HSS values tended to diverge for very long cracks with the stress demands being highest for the configuration with the thinnest angles and plate.

Similar trends were observed for computed J-Integral values from contours surrounding the tip of the horizontal crack, at the tension face of the web (Fig. 1-13c). Calculated J-Integral values for retrofitted models with $\frac{1}{2}$ -in. cracks fell between those calculated for models with 1- and 8-in. cracks, with the highest value corresponding to the models with 1-in. cracks. This trend was similar to that observed in Fig. 1-13a and 13b for the HSS, and suggests that the potential for crack growth increased with crack length for relatively short cracks (less than 25-mm or $\frac{1}{2}$ -in. long). For longer cracks, the computed J-Integral values suggest that the potential for crack growth decreased with increasing crack length, and was lowest for the configuration with the longest crack and thinnest angles and plate. This was an important finding considering that the angles-with-plate retrofit measure does not provide any direct connectivity between the connection plate and the flange. The main driving force for the horizontal crack (HSS Path #2) is induced by bending moments in the girder web, caused by the distortion of the web-gap

region. The addition of the angles and back plate in the web-gap region prevent the distortion of the girder web and consequently the distortion-induced bending moments in the web-gap. The stiffness of the back plate allows the distribution of the out-of-plane forces over a much larger area, outside of the web-gap, which causes a significant reduction in the driving force affecting the horizontal crack.

The results from the parametric study show that the effectiveness of the angles-with-plate retrofit measure, quantified in terms of the HSS and the J-Integral, was not very sensitive to crack length. Of the two types of crack studied, the effectiveness of the retrofit measure was most sensitive to crack length for the horizontal crack near the web-to-flange weld. These results indicate that this type of repair should be equally effective for cracks with various lengths, and that the most effective configurations are likely to be those with very stiff elements.

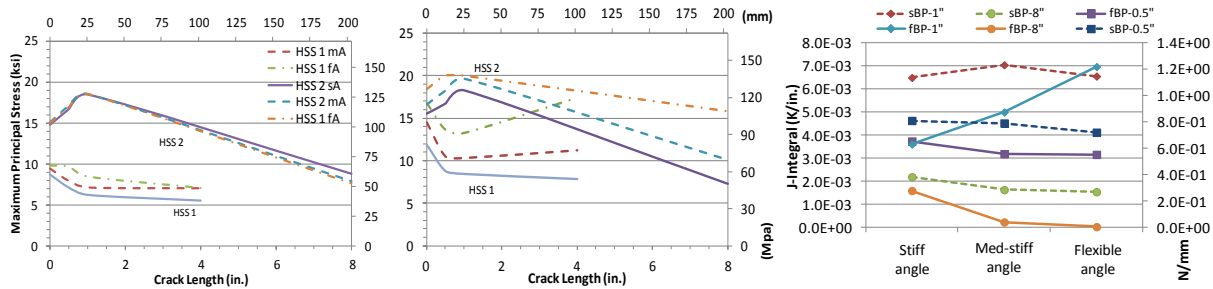


Figure 1-13: Peak demand at web-gap region vs. crack length for retrofitted specimens a) HSS for stiff back plate configurations b) HSS for flexible back plate configurations, c) J-Integral for various back plate configurations.

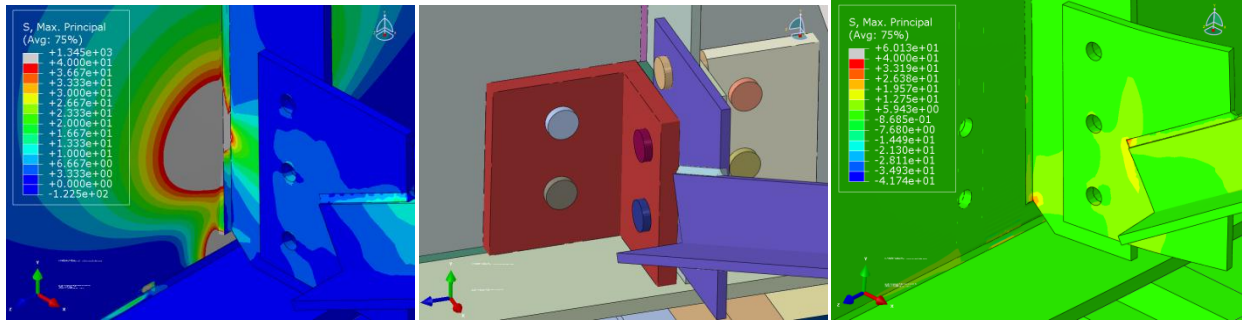


Figure 1-14: a) computed stresses without retrofit b) angle retrofit configuration c) computed stresses with retrofit.

Experimental Program

The goal of the experimental study was to confirm the findings of the finite element simulations by evaluating the fatigue-crack propagation life of steel girders repaired using two different retrofit measures. The two retrofits measures evaluated experimentally in this study were crack stop holes, and the angles-with-plate repair.

In the web-gap region of an existing bridge, the top flange of a girder is restrained from lateral motion by the bridge deck, while the bottom flange is free or nearly free to move in the out-of-plane direction. In the laboratory, it is difficult to replicate the same boundary conditions that exist in a bridge when performing a component test. The subassemblies evaluated in this study were placed upside down (Fig. 1-7) meaning that the unrestrained flange was at the top of the subassembly. One of the effects of attaching the specimen to the reaction floor in this manner is that gravity load bending stresses are eliminated from the girder web, leaving only the out-of-plane demands imposed by the cross-frame. Consequently, the stress field imposed on the specimens was more representative of the behavior expected near inflection points of bridges. The combined effects of bending and out-of-plane stresses are being investigated in a companion study using a reduced-scale bridge model.

The web-gap region of the girder subassembly was loaded under a constant stress range while the propagation of fatigue cracks was monitored. Given the characteristics of the stress field at the web-gap region, experimental results provided insight about crack propagation behavior under the combined effects of fracture modes 1 and 3 (opening and shear). The experimental results also allowed for direct comparisons between the two repair methods.

Specimen dimensions

The girder subassemblies were built-up I shape sections with a height of 918-mm (36-in.). The thickness of the web was 10-mm ($\frac{3}{8}$ -in.) and web height was 876-mm ($34\frac{1}{2}$ -in.). The top and bottom flanges had a width of 279-mm (11-in.), and thicknesses were 25-mm (1-in.) and 16-mm ($\frac{5}{8}$ -in.), respectively. The connection plate in the middle of the girder was attached to the web with a 5-mm ($\frac{3}{16}$ -in.) weld. The CP had a thickness of 10-mm ($\frac{3}{8}$ -in.), a width of 127-mm (5-in.), and a height of 873-mm ($34\frac{3}{8}$ -in.). The CP had a cropped end of 32-mm ($1\frac{1}{4}$ -in.). There was a 3-mm ($\frac{1}{8}$ -in.) gap between the CP and bottom flange. At the top of the girder, the CP was bearing against the inside face of the top flange, without any welded connection. At each end of the girder, on both sides of the web, stiffeners were welded to the web and both flanges. The stiffener dimensions at the ends of the girder were 10x876x127 mm ($\frac{3}{8} \times 34\frac{1}{2} \times 5$ in.). The girder subassembly was attached to the laboratory floor with C5x9 channels (Fig. 1-9). The channels were connected to the girder through fully-tightened 19-mm ($\frac{3}{4}$ -in.) diameter A325 structural bolts. The bottom flange was connected to the channels with bolts at a spacing of 1 ft. A cross-frame connected the specimen to the actuator. The cross-frame consisted of three L76x76x10-mm ($L3 \times 3 \times \frac{3}{8}$ -in.) angles, with an X-shape configuration and a horizontal

member. The cross frame was connected to a WT section used to stabilize the free end of the cross frame and to prevent warping and bending of the frame while loading the specimen.

Material properties

All the plates used to fabricate the built-up section were grade A36 steel. Coupons were taken from the web, and both the top and bottom flanges after the test was concluded. Measured yield strengths are summarized in Table 1-3. The web coupons (#1-3) had a 23-cm (9-in.) test length while the flange coupons (#4-9) had a 5.7-cm (2-¹/₄-in.) test length in accordance with ASTM E8/E8M (2009). The difference in tensile coupon dimensions accounts for the variation in percentage elongation in the test results.

Table 1-3: Tensile Coupon Tests

Coupon #	Description	F_y, MPa (ksi)	F_u, MPa (ksi)	E, GPa (ksi)	% Elongation
1	Web	372 (54)	524 (76)	192 (27900)	19
2	Web	352 (51)	531 (77)	216 (31400)	20
3	Web	379 (55)	531 (77)	205 (29800)	22
	Average:	365 (53)	531 (77)	205 (29700)	20
4	Thinner FL	331 (48)	490 (71)	172 (25000)	38
5	Thinner FL	331 (48)	483 (70)	196 (28500)	37
6	Thinner FL	345 (50)	490 (71)	210 (30400)	39
	Average:	338 (49)	490 (71)	193 (28000)	38
7	Thicker FL	317 (46)	483 (70)	218 (31600)	39
8	Thicker FL	310 (45)	483 (70)	222 (32200)	39
9	Thicker FL	324 (47)	483 (70)	216 (31400)	37
	Average:	317 (46)	483 (70)	218 (31700)	38

Instrumentation

The specimens were instrumented with linear variable differential transformers (LVDTs) and with strain gages, in locations shown in Fig. 1-15. Two strain gages were located behind the connection plate at the top and bottom of the web (Gages 5-7). Another two were located on the right side of the connection plate (Gages 4-6) (Fig. 1-15). The stress range was defined on the

basis of the readings from strain gage 4, located 17-mm ($\frac{5}{8}$ -in.) to the right of the CP. This location was selected because the computer simulations showed that the stress field was nearly constant in this region and the stress was considered to be representative of the bending stress induced by the out-of-plane motion in the web-gap. The measured stress range under the applied load recorded by gage 4 was 196 MPa (28.5 ksi).

The LVDTs were placed to measure the out-of-plane deflections at three different locations on the center line of the girder. The first LVDT was placed at the top flange, the second at the midsection of the web, and the third directly behind the bottom end of the CP. Good agreement was found between the deflected shapes computed in the simulations and the experimental measurements (Fig. 1-16). As shown in Fig. 1-16, the computed deflections for the nominal force range were lower in magnitude than those measured, but when scaled to match the measured deflection range at the top of the girder the slope of the deflected shape at the center of the girder matched the measured deflected shape very closely.

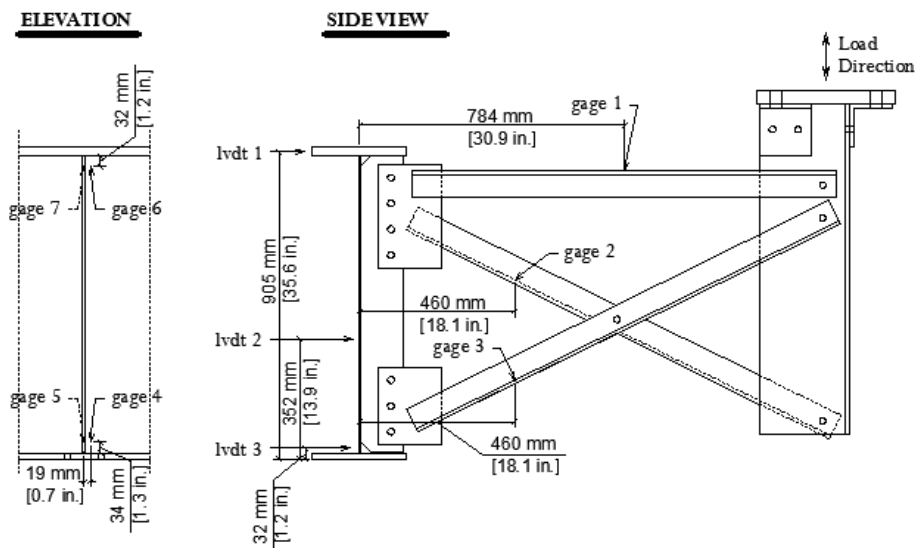


Figure 1-15: Instrumentations on 9-ft girder specimen.

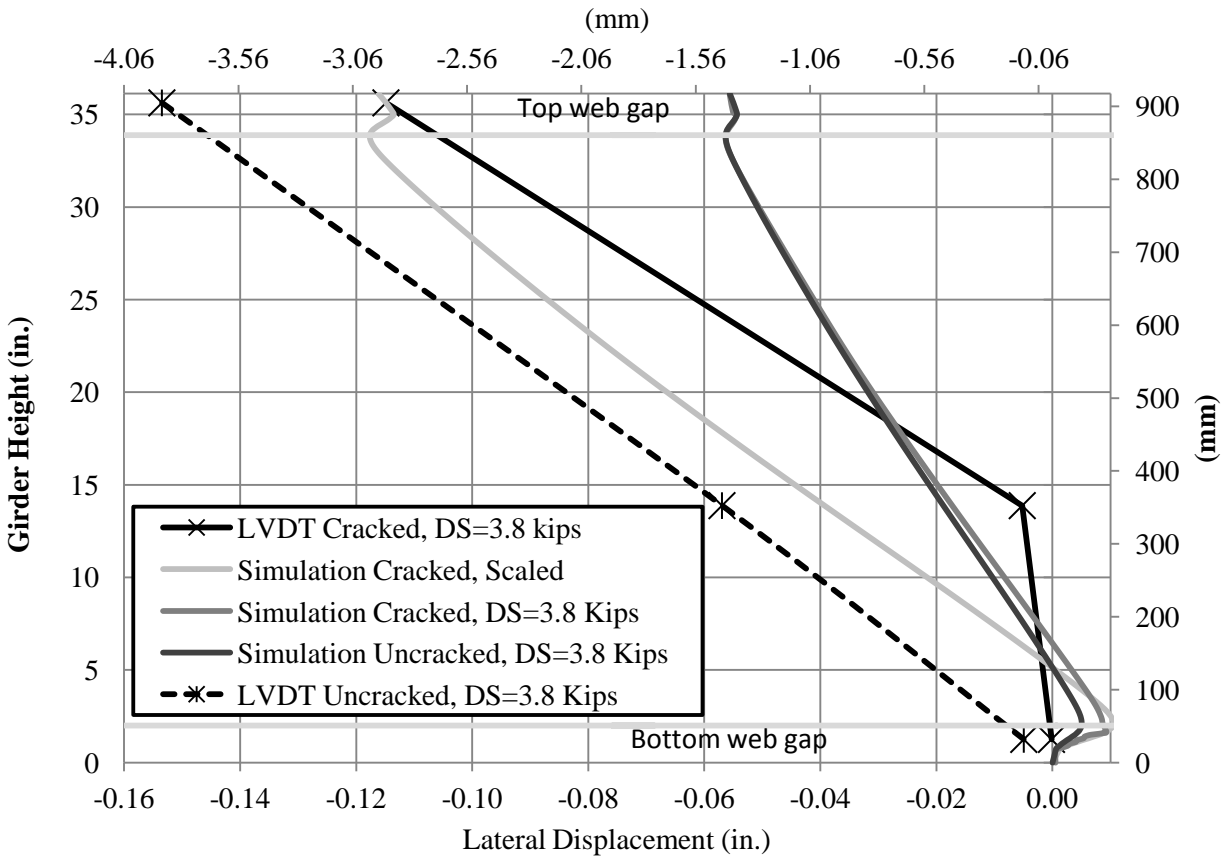


Figure 1-16: Comparison between LVDT readings and computed deformations

Gages reading comparison with simulation model

Figure 1-17 shows a comparison between strain gage readings and simulation results. The computed strains shown in the figure represent average values over the area occupied by the gages. The gage readings were slightly higher than the simulation values, which is consistent with the results for the deflected shapes.

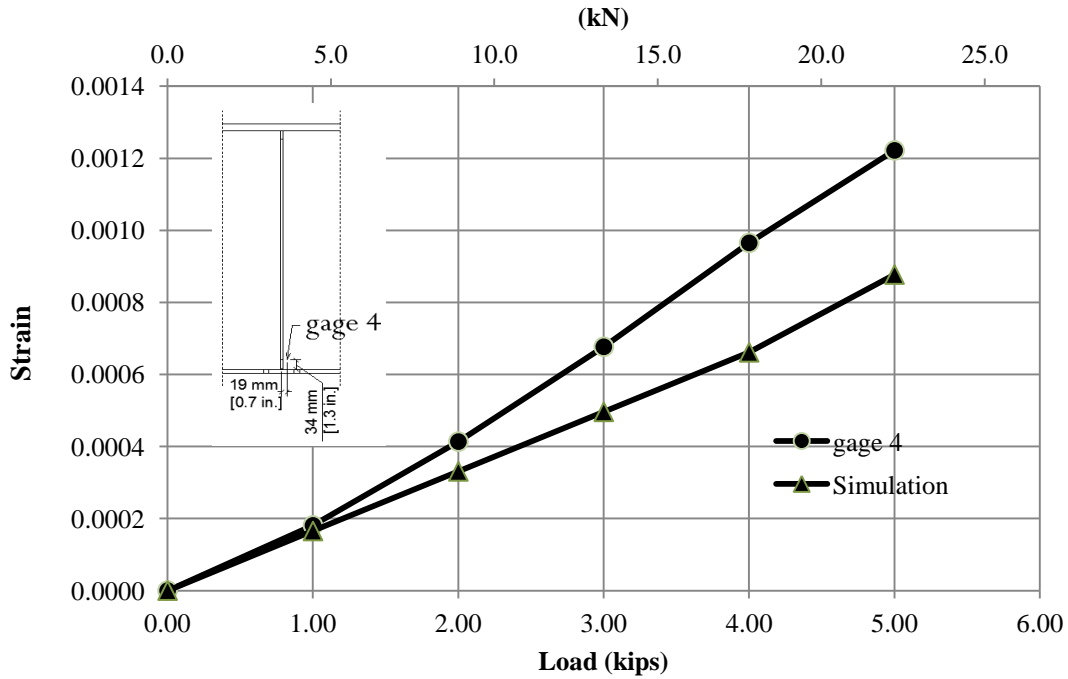


Figure 1-17: Strain gage readings compared with simulation model results.

Test procedure

Specimens were subjected to cyclic loading applied to induce out-of-plane distortion of the web-gap. The maximum load applied was 20-kN (4.6-kip) and the minimum was 3.6-kN (0.8-kip). The tests were performed using two different actuators, with the frequency of loading limited by the capacity of the servovalve of the hydraulic actuator that was employed. The loading rates for the two actuators were 0.5 and 2 Hz. Crack growth was monitored periodically. Test trials were stopped after repaired specimens exceeded the equivalent of infinite fatigue life without a measurable increase in fatigue crack length (Fig. 1-21) or when a large increment in crack length was reached. In this study infinite fatigue life of a repaired specimen was defined as the number of cycles in the S-N curve of the AASHTO LRFD Bridge Design Specification

(AASHTO 2007) corresponding to a Category A detail (approximately 1.2 million cycles) for the experimentally measured stress range 197 MPa, (28.5 ksi).

The experimental program is summarized in Table 1-4. Three specimens were evaluated with a total of 14 different test trials. Specimen 1 had a pre-drilled horizontal crack with a length of 38-mm (1-1/2-in.) at a distance of 17-mm (5/8-in) from the top of the bottom flange. Specimen 1 was subjected to cyclic loading to monitor the crack progression.

Table 1-4: Experimental Program

Specimen	Test Trial	Configuration
1	1	Pre-Cracked, Unretrofitted
2	1	Un-cracked, Unretrofitted
2	2	Cracked, Angles with Plate Retrofit Bottom Web-Gap
2	3	Cracked, Angles with Plate Retrofit Bottom and Top Web-Gap
2	4	Cracked, Crack-Stop Hole Retrofit
2	5	Cracked, Angles with Plate Retrofit Bottom and Top Web-Gap
3	1	Pre-Cracked, Unretrofitted
3	2	5.1-cm (2-in.) Horizontal Crack, Retrofitted
3	3	Cracked, Unretrofitted
3	4	10.2-cm (4-in.) Horizontal Crack, Retrofitted
3	5	Cracked, Unretrofitted
3	6	15.2-cm (6-in.) Horizontal Crack, Retrofitted
3	7	Cracked, Unretrofitted
3	8	20.3-cm (8-in.) Horizontal Crack, Retrofitted

Specimen 2 was first tested in the uncracked configuration. The first trial consisted of loading the specimen while periodically monitoring the crack progression without any type of retrofit measure. After significant damage had been sustained, a second test trial was conducted in which the angles-with-plate retrofit measure was applied to the bottom web-gap while monitoring crack growth periodically. During trial 2 for Specimen 2, a crack was observed at the top web-gap. A third test trial was conducted in which the specimen was repaired with the

angles with retrofit repair at the top and bottom web-gaps. A fourth trial was conducted in Specimen 2 in which crack-stop holes were drilled and the angles with plate repair was removed to determine the number of cycles to crack re-initiation under the same loading range. Finally, the fifth trial involved reapplying the angle retrofit to the bottom and top web-gaps.

Specimen 3 was tested in a similar manner to Specimen 2 but with a greater number of test trials. Trial 1 consisted of growing the horizontal bottom flange-to-web crack to a length of 5.1-cm (2-in.). When the crack reached this length, the angles-with-plate retrofit was applied in trial 2. This pattern was followed in the next six trials by growing the horizontal flange-web crack to lengths of 10.2-cm (4-in.), 15.2-cm (6-in.), and 20.3-cm (8-in.) and applying the retrofit after each of these crack lengths were reached. Throughout all 8 trials, the cracks and specimen were inspected periodically for growth and initiation.

Retrofit Measures

As indicated, two different retrofit measures were evaluated experimentally. The first was the angles-with-plate retrofit, and the second consisted of drilling crack-stop holes at the tips of the cracks, a retrofit measure that is widely employed in steel bridges.

Angles with Plate Retrofit Measure

The angles with plate retrofit measure was devised with the intention of reducing the stress demand at the welded connection between the connection plate and the web of the girder, preventing further growth of horseshoe-shaped cracks around the CP. The back plate was added with the goal of distributing the out-of-plane force transferred by the cross frame over a larger area of the web, reducing the stress demand at the connection between the web and the flange of the girder, preventing further growth of the horizontal crack commonly found at that location.

The angle and cover plate dimensions evaluated experimentally were L152x152x19-mm (L6x6x $\frac{3}{4}$ -in.) and 457x457x19-mm (18x8x $\frac{3}{4}$ -in.), respectively (Fig. 1-18). Angles were connected to the web and the connection plate with two bolts on each leg (Fig. 1-19). A 10-mm ($\frac{3}{8}$ -in.) thick shim plate was placed between the CP and the angle to prevent any chamfering or grinding of the edge of the angles. The angles and the back plate were removed every 250,000 cycles to inspect the web-gap region and measure crack growth.

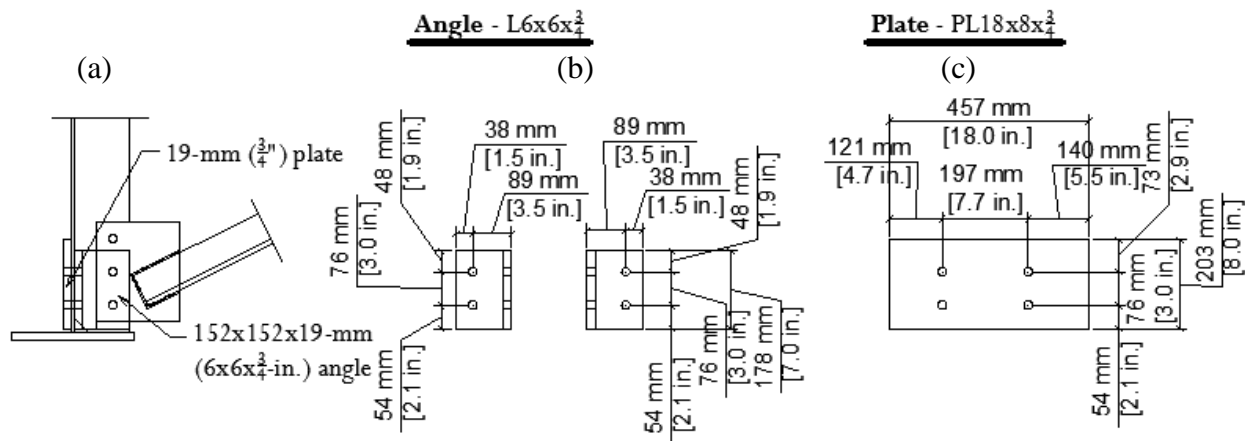


Figure 1-18: Dimensions of angles and plate evaluated experimentally. a) side view, b) angle dimensions, c) plate dimension



Figure 1-19: Angle retrofit with plate a) back plate, b) angles

Crack stop holes

Crack stop holes were selected to have a diameter of 21-mm ($^{13}/_{16}$ -in.), similar to the hole size used for the angles with retrofit repair. This diameter was chosen given the severe level of damage at the web-gap region when the holes were drilled. Drilling holes with the same diameter as those commonly drilled in bridge girders under the circumstances would have resulted in excessive weakening of the web-gap region. Furthermore, there are many situations in which the constraints imposed by the geometry of the web-cross frame connection or the location of the cracks present a similar problem to engineers in charge of repairing fatigue damage.

The crack-stop holes were drilled so that the edge of the hole would coincide with the corresponding crack tip. When two cracks were found closely located to each other a single crack stop hole was drilled to encompass both crack tips. Crack stop holes were not drilled at cracks that had stabilized in the unretrofitted configuration. The hole placement in the bottom and top web-gaps of specimen 2 are shown in Fig. 1-20. As shown in Fig. 1-20 some cracks intersected others; for example, horizontal cracks on the front and back of the web. In that case, crack stop holes were placed on the longer cracks and the smaller diameter holes were drilled at the tips of the shorter cracks. The smaller holes had a diameter of 6-mm ($^{1}/_{4}$ -in.). The diameter of the crack stop holes was 21-mm ($^{13}/_{16}$ -in.) and they were drilled using a hole saw with guide.

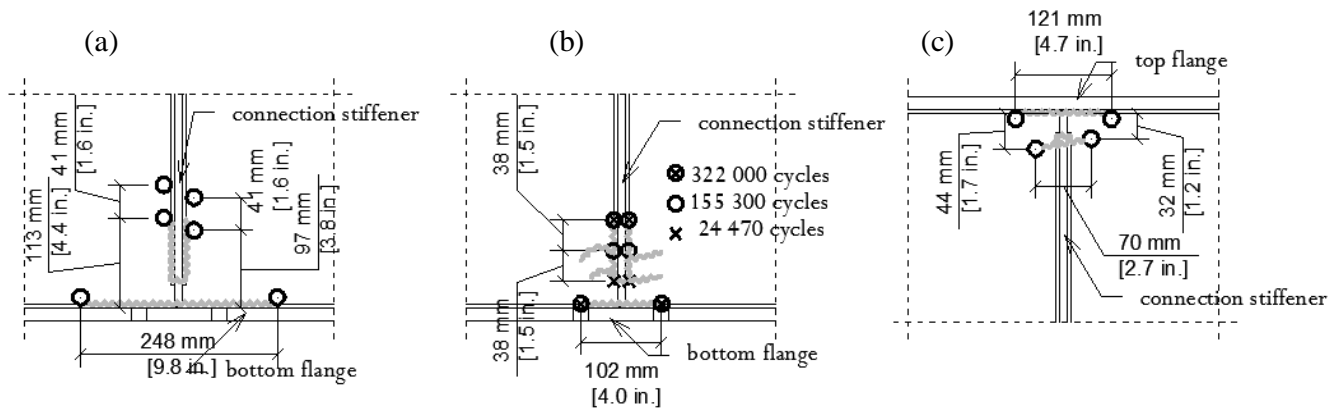


Figure 1-20: a) Crack stop holes in bottom web-gap region specimen 2, b) Crack progression at the bottom web-gap region of specimen 2, un-retrofitted, c) Crack stop holes at the top web-gap region

Experimental results

As described in the experimental program section a total of fourteen test trials were performed on the beam subassemblies. Crack progression for the various test trials is summarized Table 1-5.

Prior to loading Specimen 1 a 38-mm (1-¹/₂-in.) horizontal crack was pre-cut in the web-gap region, between the edge of the connection plate and the flange weld. The main purpose of the trial conducted with this specimen was to explore the evolution of the crack propagation pattern and to provide data for calibrating the FE models. Test trial 1 was concluded after 740,000 cycles, and no retrofit measures were evaluated in this specimen. The crack pattern, shown in Fig. 1-10a, was similar to that found in Specimen 2. A fatigue crack developed at the toe of the CP-to-web fillet weld, similar to the crack that developed at the fillet weld of Specimen 2 (Fig. 1-10b, and 1-20b). Consistent with the results from the FE simulation (Fig. 1-10a), the ends of the pre-cut horizontal crack grew towards the bottom flange.

Five different test trials were conducted using Specimen 2. The first trial was without any retrofit or pre-existing crack, and crack growth was monitored for a total of 490,000 cycles.

The crack progression is illustrated in Fig. 1-20. As shown, the first crack in the specimen was noted at 22,700 cycles, located at the toe of the weld in the bottom web-gap region. Cracks continued to grow as shown in Fig. 1-20b with a second crack developing at the web-to-flange connection, in the horizontal direction. At the conclusion of the first trial the specimen had the crack pattern shown in Fig. 1-20a with a few secondary cracks radiating from the CP-to-web weld in the horizontal direction. At 490,000 cycles the main crack along the CP-to-web weld had a length of approximately 101-mm (4-in.) in the vertical direction, while the horizontal crack along the web-to-flange connection had a length of 203-mm (8-in.).

The remaining trials conducted with the second specimen were carried out to evaluate the performance of retrofit measures. During the second trial, which extended for a total of 1,225,860 cycles, two angles and a cover plate were used to reinforce the bottom web-gap region. During this trial, two new cracks initiated in the top web-gap region. At the end of the trial, an 83-mm (3-¹/₄-in.) long horizontal crack had formed at the top web-gap, following the tip of the flange-to-web weld, and a 29-mm (1-¹/₈-in.) vertical crack had propagated down from the top of the connection plate-to-web weld.

During the third trial, angles and a connection plate were attached to the top web-gap region. The specimen underwent a total of 1,250,740 cycles in this configuration. At the end of the third trial the cracks in the bottom web-gap exhibited no additional crack growth, but the horizontal crack at the top web-gap region extended an additional 25-mm (1-in.) and the vertical crack gave rise to a secondary crack behind the stiffener. The orientation of the secondary crack was almost horizontal and the length at the end of the trial was approximately 51-mm (2-in.).

A fourth trial was carried out to evaluate the performance of crack-stop holes compared with that of the “angles and plate” repair. A total of 10 holes with a diameter of 19-mm (³/₄-in.)

and 4 holes with a diameter of 6-mm ($1/4$ -in.) were drilled. At the end of this test trial, which lasted a total of 39,720 cycles, the bottom horseshoe-shaped crack had grown an additional 70-mm ($2\text{-}3/4$ -in.) and the bottom horizontal crack extended an additional 13-mm ($1/2$ -in.). For the fifth trial, the angles and back plate were again applied to the top and bottom web-gap regions and the specimen was subjected to 1,238,300 cycles. After this test, the specimen was inspected and no crack growth was observed. Experimental results from the various test trials are compared on the basis of the AASTHO S-N Curve in Figure 1-21.

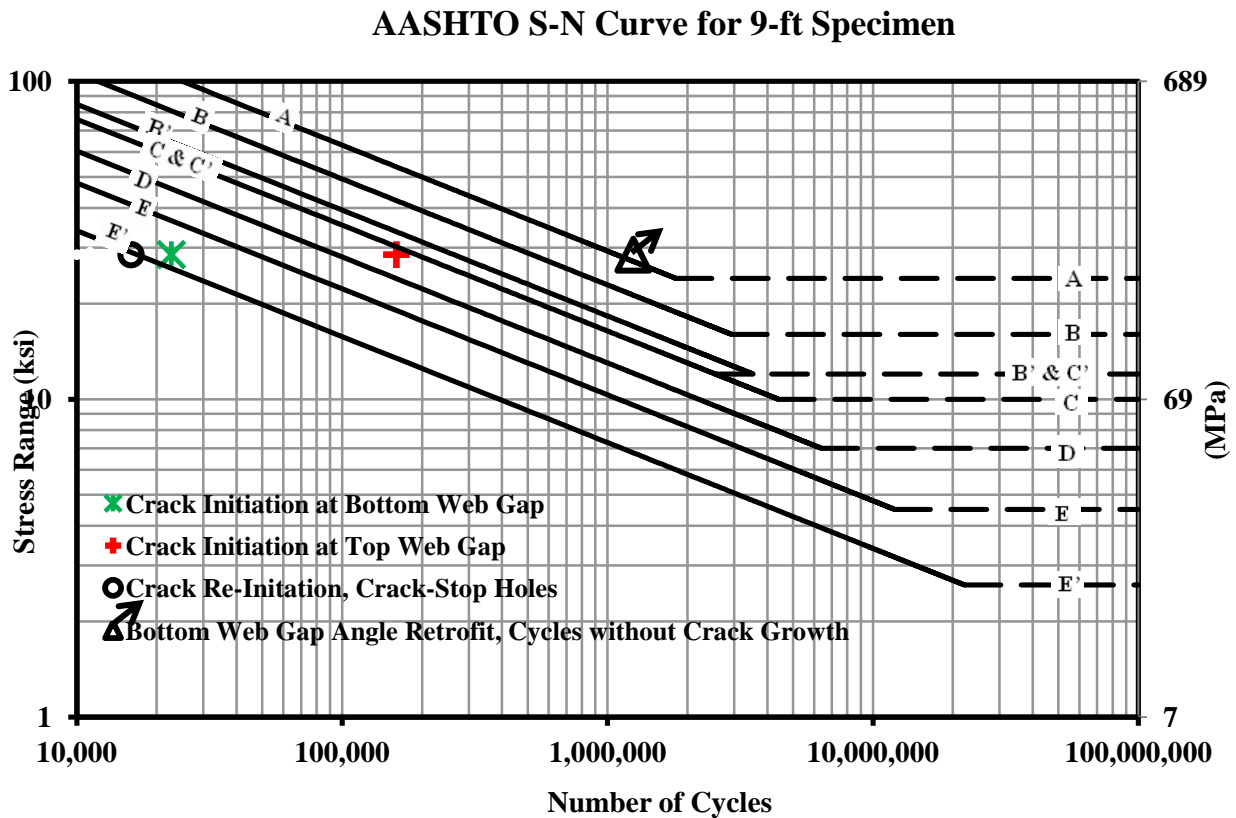


Figure 1-21: Experimental results for specimen 2 trials.

Eight trials were conducted on Specimen 3 following the same loading protocol used for Specimen 2. The main differences between specimens 2 and 3 were the lack of crack-stop holes

and the fact that no angles-with-back plate retrofit measure was applied to the top web-gap region of Specimen 3. The reason for the latter was that there was no significant crack growth in the top web-gap of Specimen 3.

The main goal of the trials in Specimen 3 was to study the effectiveness of the angles-with-plate retrofit measure for different crack lengths. In trial 1, the girder was subjected to cyclic loading without retrofit. The first crack, with a length of 10-mm ($\frac{3}{8}$ -in.), was observed in the web toe of the bottom stiffener-web weld at 73,000 cycles. At 150,000 cycles, a 2-mm ($\frac{1}{16}$ -in.) crack was observed at the toe of the bottom flange-web weld. The cracks were allowed to grow in the unretrofitted configuration until the horizontal web-flange crack reached 51-mm (2-in.) at 349,000 cycles. The horseshoe crack reached 51-mm (2-in.) also, and spider cracks that branched out of the horseshoe-shaped crack in the horizontal direction, on either side of the stiffener, reached 13-mm ($\frac{1}{2}$ -in.).

For the second trial, the angles-with-back plate retrofit was applied to the bottom web-gap and the specimen was cycled for an additional 1.2 million cycles. During the second trial, no crack growth was observed in the horseshoe-shaped crack around the stiffener or in the horizontal crack at the bottom flange-web weld. Trial 3 consisted of a total of 71,700 cycles in the unretrofitted configuration. During trial 3 the horizontal crack grew to 102-mm (4-in.), the spider cracks grew to 19-mm ($\frac{3}{4}$ -in.), and the horseshoe-shaped crack showed no growth. The spider cracks propagated through the thickness of the web to the fascia side of the girder to 35-mm ($1\frac{3}{8}$ -in.).

The fourth trial for Specimen 3 was conducted with the angles-with-back-plate retrofit measure for an additional 1.2 million cycles. The specimen was inspected periodically by interrupting the loading and removing the retrofit but no crack growth was observed. Trial 5

consisted of 322,000 cycles in the unretrofitted configuration. During this trial the horizontal crack grew to a length of 152-mm (6-in.), the horseshoe-shaped crack grew to 70-mm ($2\frac{3}{4}$ -in.), and the spider cracks grew to a length of 30-mm ($1\frac{3}{16}$ -in.) and 22-mm ($\frac{7}{8}$ -in.) to the right and left of the stiffener, respectively. After 2,931,200 total cycles, a small crack was found in the top web-gap in the toe of the stiffener-web weld during trial 5 (3-mm, $\frac{1}{8}$ -in.). By the end of trial 5, this crack had grown to 10-mm ($\frac{3}{8}$ -in.). Trial 6 consisted of 1.2 million load cycles with the retrofit measure with periodic inspections. No crack propagation was observed during trial six.

In the seventh trial, the retrofit was removed and the crack growth monitored over a total of 275,000 cycles. The horizontal crack reached a length of 206-mm ($8\frac{1}{8}$ -in.) and the horseshoe-shaped crack reached 83-mm ($3\frac{1}{4}$ -in.). The right spider crack grew to 36-mm ($1\frac{3}{8}$ -in.) but the left spider crack saw no growth. The top web-gap crack also showed no signs of growth. Additionally, on the stiffener side of the girder, the horizontal crack propagated through the thickness of the web to a length of 206-mm ($8\frac{1}{8}$ -in.), where it had only been observed on the fascia side of the girder before. The eighth trial was the final trial conducted on the specimen and again involved the application of the angles-with-back plate retrofit. After 1.2 million cycles, no growth was observed in any of the cracks in the girder.

The measured displacements from the top and middle LVDTs are illustrated in Figures 1-27 and 1-28, respectively. The graphs show that the increase in top flange and web displacement was slight at the beginning of the test trials, and increased as the tests progressed. When the angles-with-back plate retrofit measure was applied, there was a marked decrease in displacement at all four retrofit applications. The data collected from gage 1 (gage on the west lateral brace angle) shows that there was an increase in strain throughout the testing of specimen 3, with some sharp decreases at the points where the angles-with-back plate retrofit measure was

applied (Fig. 1-29). The data was only reported up to the end of trial 6 because the gage became damaged at this point.

The cumulative crack growth observed in specimens 2 and 3 is illustrated in Fig. 1-22 through 1-24. Figure 1-22 shows that crack growth in Specimen 2 only occurred in the horizontal web-flange crack in the top web gap. However, most of this growth took place when there was only an angle-with-plate retrofit in the bottom web gap. The effectiveness of the angle-with-plate retrofit was also evident in Specimen 3. Figures 1-23 and 1-24 clearly show that when the retrofit measures were in place, there was no measurable growth in any of the existing cracks. It can also be noted from the graphs that some cracks tended to grow exponentially at some points (as would be expected from cracks of Modes I-III) but then slowed in their growth due to the softening of the girder subassembly. As shown in Figures 1-25 and 1-26, the crack growth in the unretrofitted configuration occurred as expected. The only trend that seems inconsistent is perhaps the growth of the horseshoe-shaped crack growth prior to Trial 2 (Fig. 1-26). During this period, the vertical horseshoe-shaped cracks ceased growth; however, this can be attributed to the large growth in the horizontal crack (Fig. 1-25). Figures 1-22 through 1-24 also show that the angles-with-plate retrofit measure was equally effective for various crack lengths, ranging from very small to significantly large. This is an important consideration because it simplifies the implementation of this retrofit by allowing the use of a single-size configuration for all cracks of the same type observed in a bridge, regardless of crack length.

Table 1-5: Crack growth

Specimen/ Trial	Retrofit Measure/Observation	Number of Cycles - Trial	Number of Cycles - Specimen	Crack Location and growth, mm (in.)			
				<i>Bottom Horiz.</i>	<i>Bottom Horseshoe</i>	<i>Top Horiz.</i>	<i>Top Horseshoe</i>
1/1	<i>No Retrofit / Crack initiation</i>	250,000	250,000	0 (0)	6 (0.3)	0 (0)	0 (0)
1/1	<i>No Retrofit / Crack growth</i>	740,000	990,000	6 (¹ / ₄)	25 (1)	0 (0)	0 (0)
2/1	<i>No Retrofit / Crack initiation</i>	24,460	24,460	0 (0)	6 (0.3)	0 (0)	0 (0)
2/1	<i>No Retrofit / Crack growth</i>	490,460	514,920	203 (8)	127 (5)	0 (0)	0 (0)
2/2	<i>Angles Bottom</i>	1,225,860	1,740,780	0 (0)	0 (0)	57 (2- ¹ / ₄)	25 (1)
2/3	<i>Angles Bottom & Top</i>	1,250,740	2,991,520	0 (0)	0 (0)	25 (1)	0 (0)
2/4	<i>Crack Stop Holes</i>	39,720	3,031,240	13 (¹ / ₂)	70 (2- ³ / ₄)	0 (0)	0 (0)
2/5	<i>Angles Bottom & Top</i>	1,238,300	4,269,540	0 (0)	0 (0)	0 (0)	0 (0)
3/1	<i>No Retrofit / Crack initiation</i>	73,000	73,000	0 (0)	10 (³ / ₈)	0 (0)	0 (0)
3/1	<i>No Retrofit / Crack growth</i>	276,000	349,000	51 (2)	41 (1- ⁵ / ₈)	0 (0)	0 (0)
3/2	<i>Angles Bottom</i>	1,200,000	1,549,000	0 (0)	0 (0)	0 (0)	0 (0)
3/3	<i>No Retrofit / Crack growth</i>	71,700	1,620,700	51 (2)	0 (0)	0 (0)	0 (0)
3/4	<i>Angles Bottom</i>	1,200,000	2,820,700	0 (0)	0 (0)	0 (0)	0 (0)
3/5	<i>No Retrofit / Crack growth</i>	322,000	3,142,700	51 (2)	19 (³ / ₄)	0 (0)	10 (³ / ₈)
3/6	<i>Angles Bottom</i>	1,200,000	4,342,700	0 (0)	0 (0)	0 (0)	0 (0)
3/7	<i>No Retrofit / Crack growth</i>	275,000	4,617,700	54 (2- ¹ / ₈)	13 (¹ / ₂)	0 (0)	0 (0)
3/8	<i>Angles Bottom</i>	1,200,000	5,817,700	0 (0)	0 (0)	0 (0)	0 (0)

Table 1-6: Crack length

Specimen/ Trial	Retrofit Measure/Observation	Number of Cycles - Specimen	Crack Location and Length, mm (in.)			
			<i>Bottom Horiz.</i>	<i>Bottom Horseshoe</i>	<i>Top Horiz.</i>	<i>Top Horseshoe</i>
1/1	<i>No Retrofit / Crack initiation</i>	250,000	0 (0)	6 (¹ / ₄)	0 (0)	0 (0)
1/1	<i>No Retrofit / Crack growth</i>	990,000	6 (¹ / ₄)	31 (1- ¹ / ₄)	0 (0)	0 (0)
2/1	<i>No Retrofit / Crack initiation</i>	24,460	0 (0)	6 (¹ / ₄)	0 (0)	0 (0)
2/1	<i>No Retrofit / Crack growth</i>	514,920	203 (8)	135 (5- ¹ / ₄)	0 (0)	0 (0)
2/2	<i>Angles Bottom</i>	1,740,780	203 (8)	135 (5- ¹ / ₄)	57 (2- ¹ / ₄)	25 (1)
2/3	<i>Angles Bottom & Top</i>	2,991,520	203 (8)	135 (5- ¹ / ₄)	84 (3- ¹ / ₄)	25 (1)
2/4	<i>Crack Stop Holes</i>	3,031,240	216 (8- ¹ / ₂)	206 (8- ¹ / ₈)	84 (3- ¹ / ₄)	25 (1)
2/5	<i>Angles Bottom & Top</i>	4,269,540	216 (8- ¹ / ₂)	206 (8- ¹ / ₈)	84 (3- ¹ / ₄)	25 (1)
3/1	<i>No Retrofit / Crack initiation</i>	73,000	0 (0)	10 (³ / ₈)	0 (0)	0 (0)
3/1	<i>No Retrofit / Crack growth</i>	349,000	51 (2)	51 (2)	0 (0)	0 (0)
3/2	<i>Angles Bottom</i>	1,549,000	51 (2)	51 (2)	0 (0)	0 (0)
3/3	<i>No Retrofit / Crack growth</i>	1,620,700	102 (4)	51 (2)	0 (0)	0 (0)
3/4	<i>Angles Bottom</i>	2,820,700	102 (4)	51 (2)	0 (0)	0 (0)
3/5	<i>No Retrofit / Crack growth</i>	3,142,700	152 (6)	70 (2- ³ / ₄)	0 (0)	10 (³ / ₈)
3/6	<i>Angles Bottom</i>	4,342,700	152 (6)	70 (2- ³ / ₄)	0 (0)	10 (³ / ₈)
3/7	<i>No Retrofit / Crack growth</i>	4,617,700	206 (8- ¹ / ₈)	83 (3- ¹ / ₄)	0 (0)	10 (³ / ₈)
3/8	<i>Angles Bottom</i>	5,817,700	206 (8- ¹ / ₈)	83 (3- ¹ / ₄)	0 (0)	10 (³ / ₈)

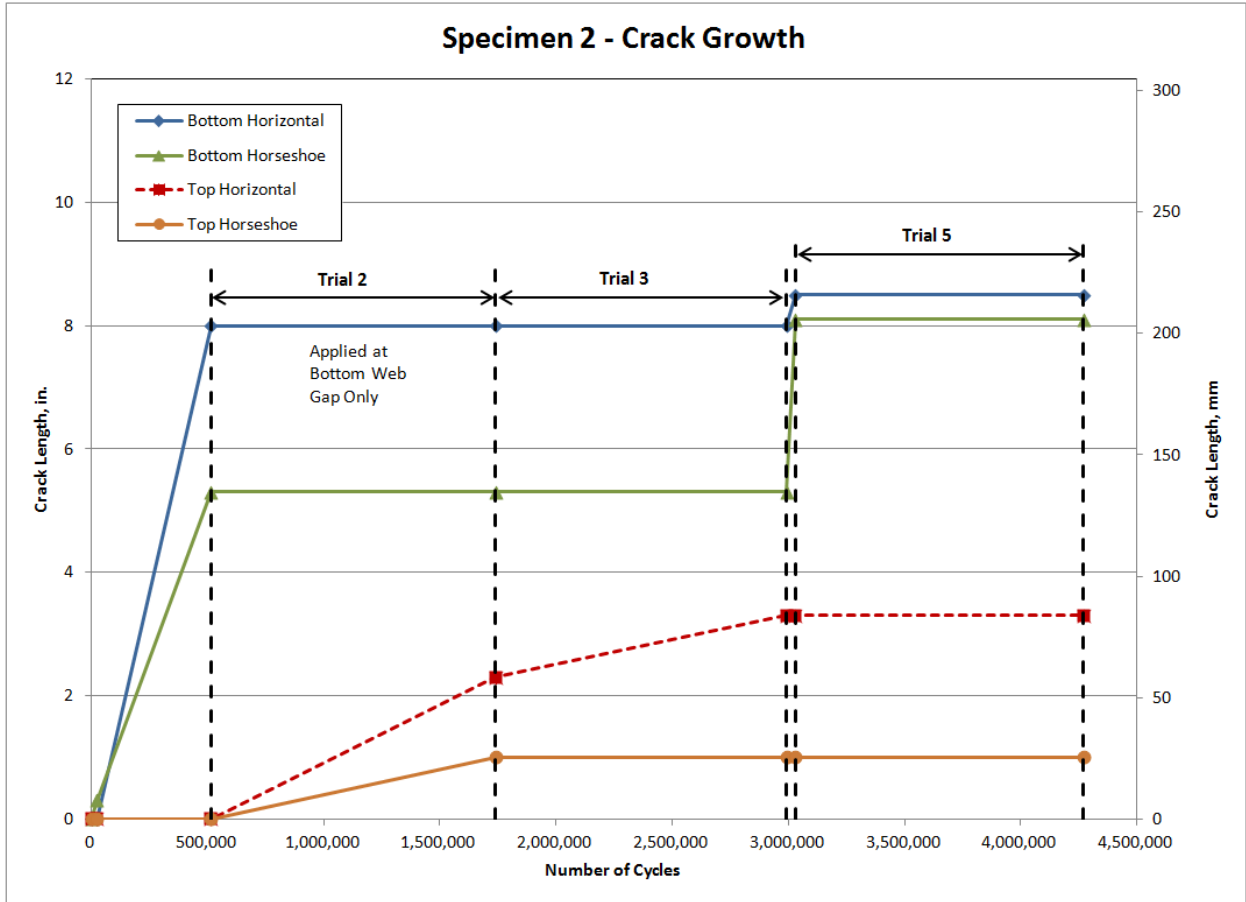


Figure 1-22: Summary of Specimen 2 crack growth

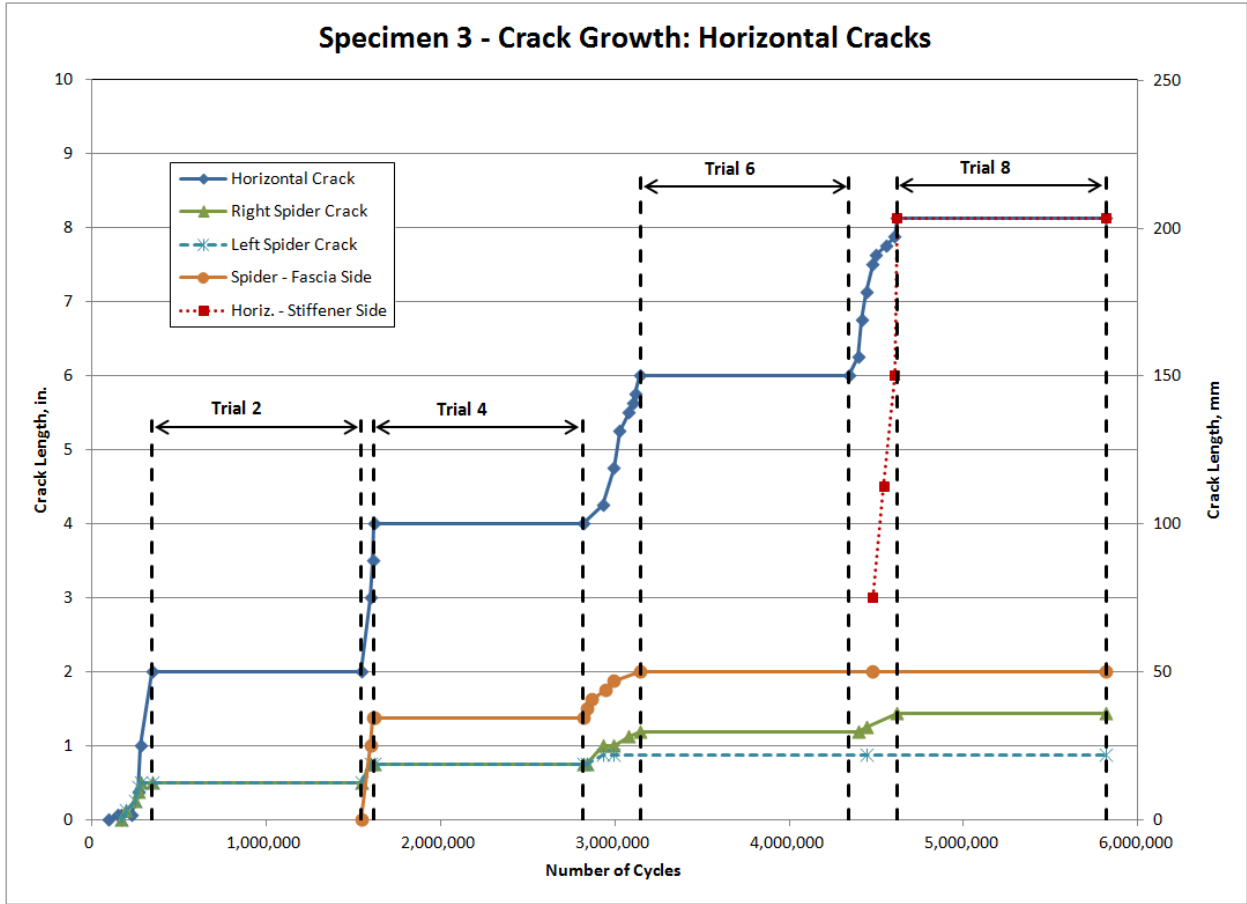


Figure 1-23 Summary of Specimen 3 horizontal crack growth

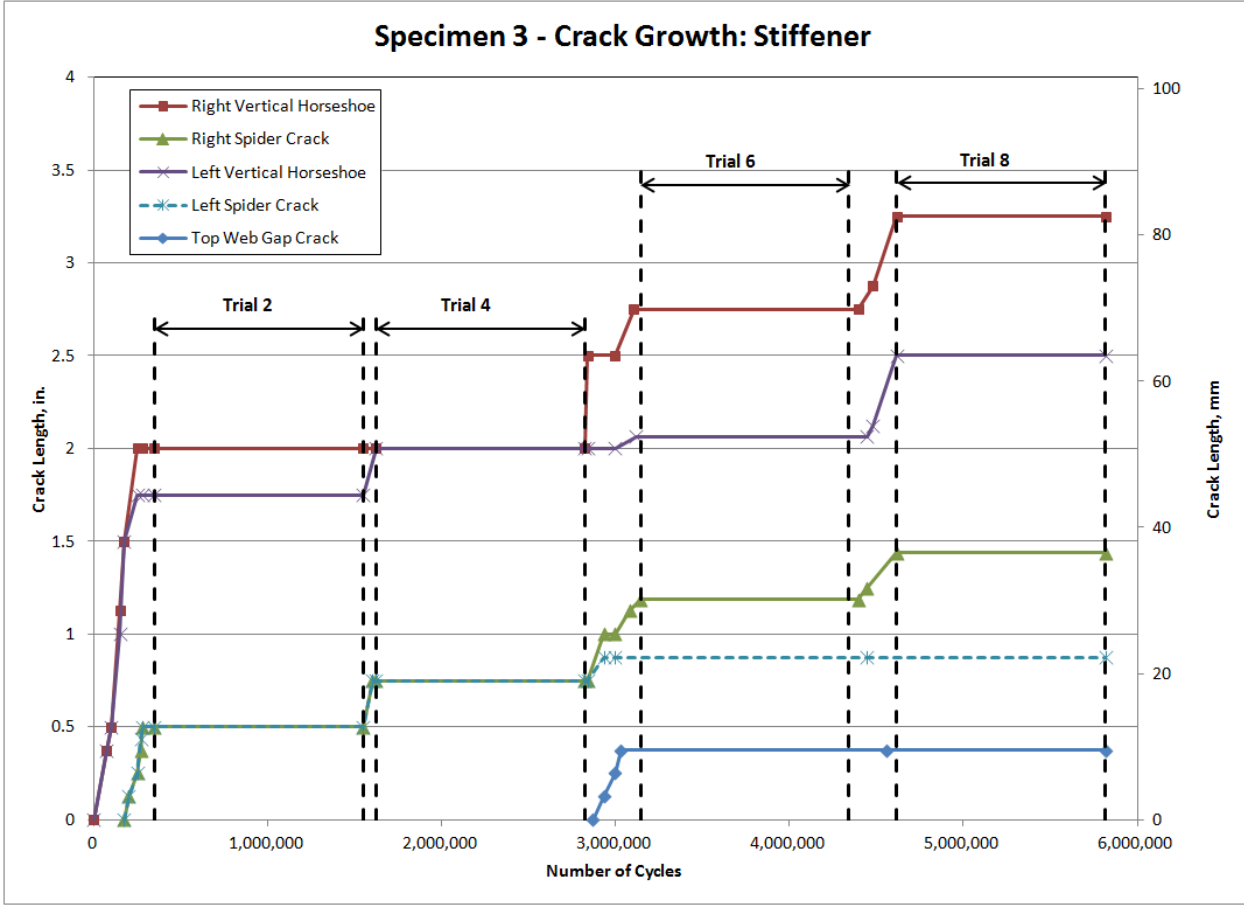


Figure 1-24: Summary of Specimen 3 stiffener crack growth

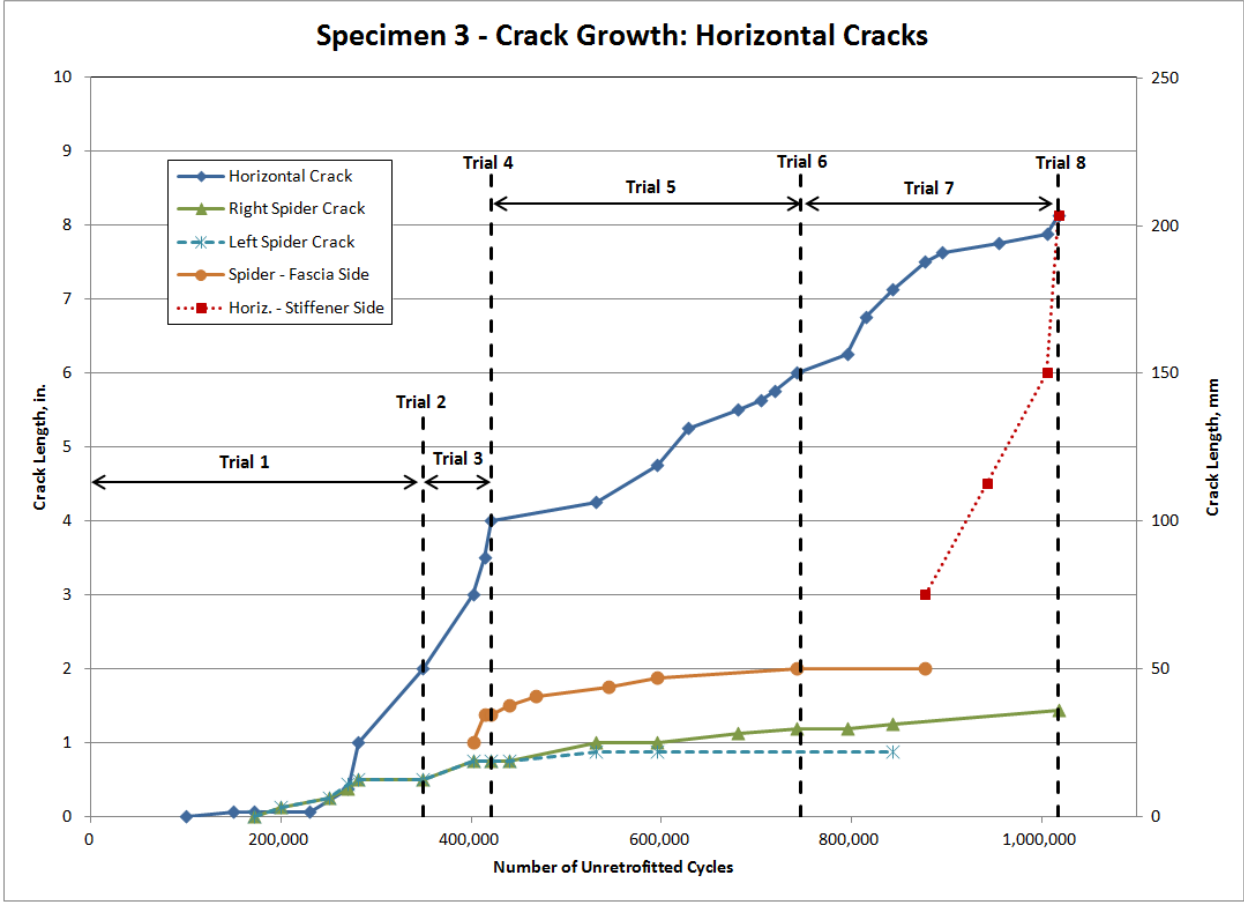


Figure 1-25: Summary of Specimen 3 horizontal crack growth in the unretrofitted configuration

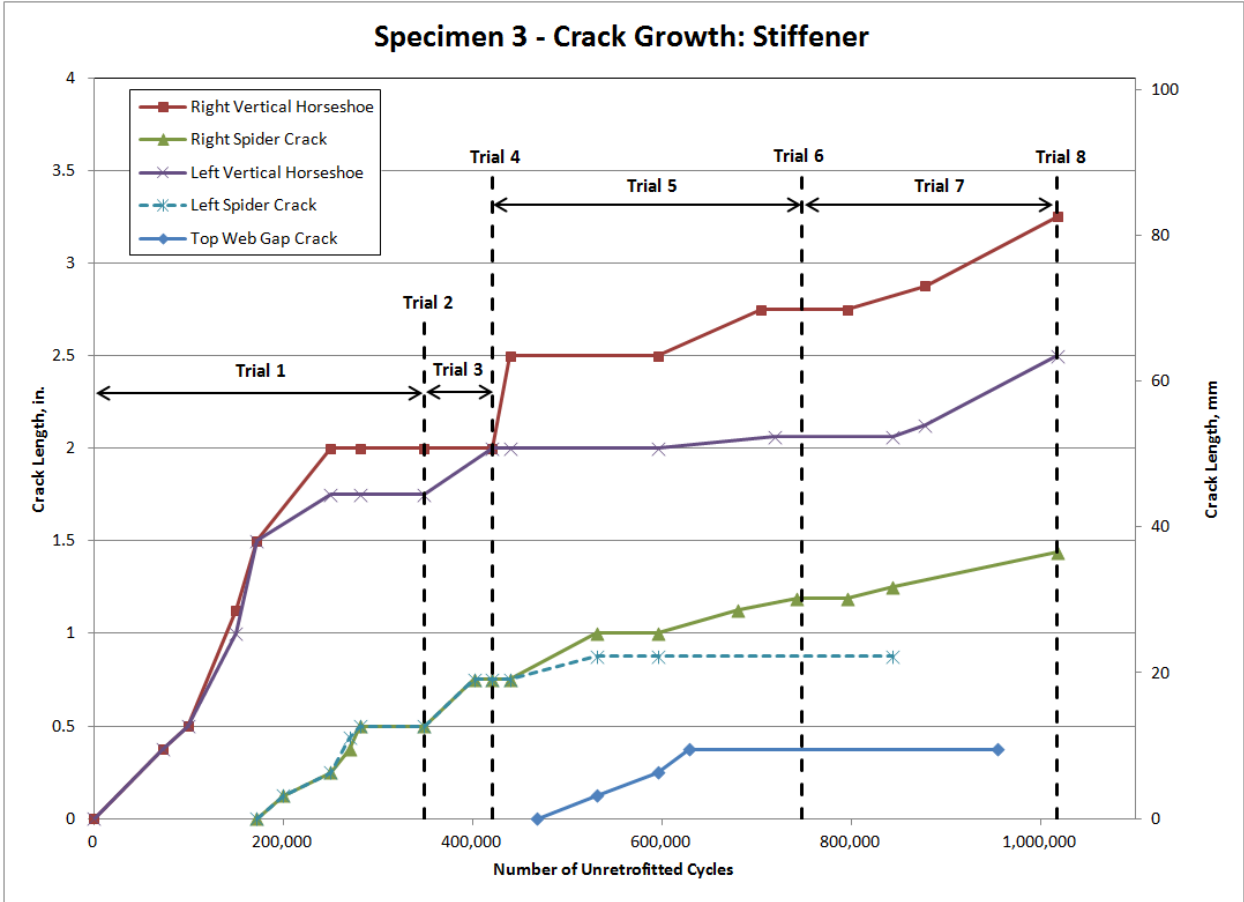


Figure 1-26 Summary of Specimen 3 stiffener crack growth in the unretrofitted configuration

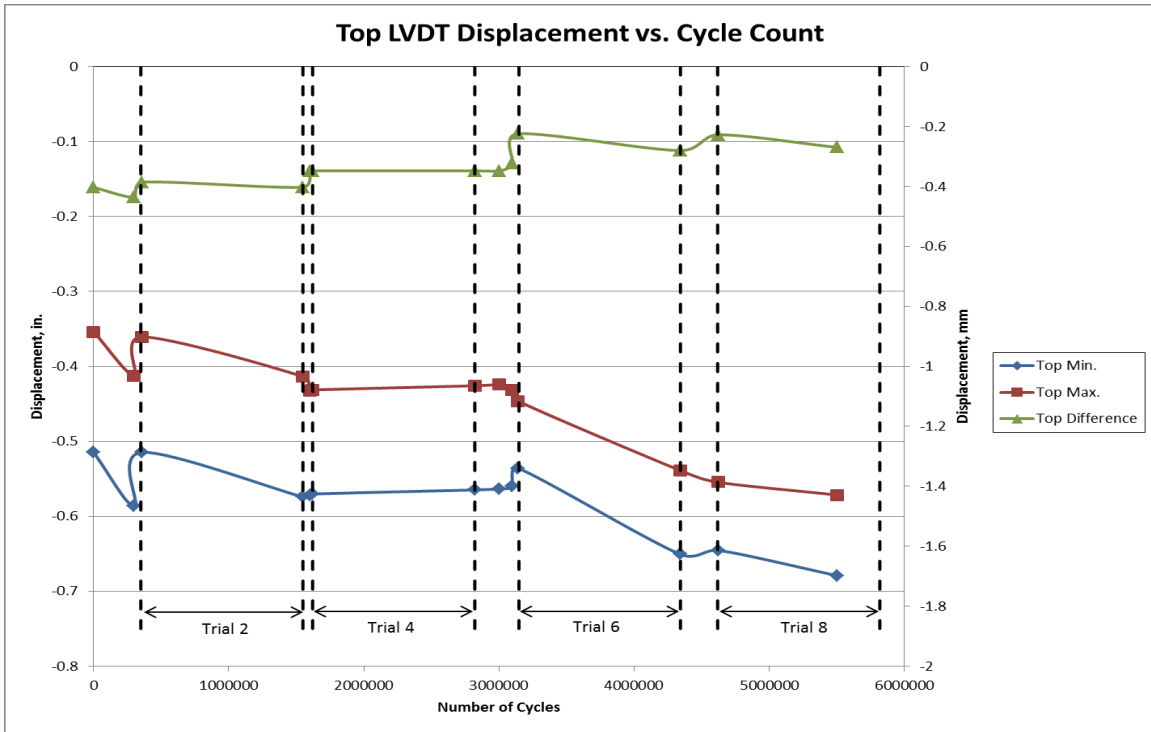


Figure 1-27: Top LVDT displacement minima and maxima

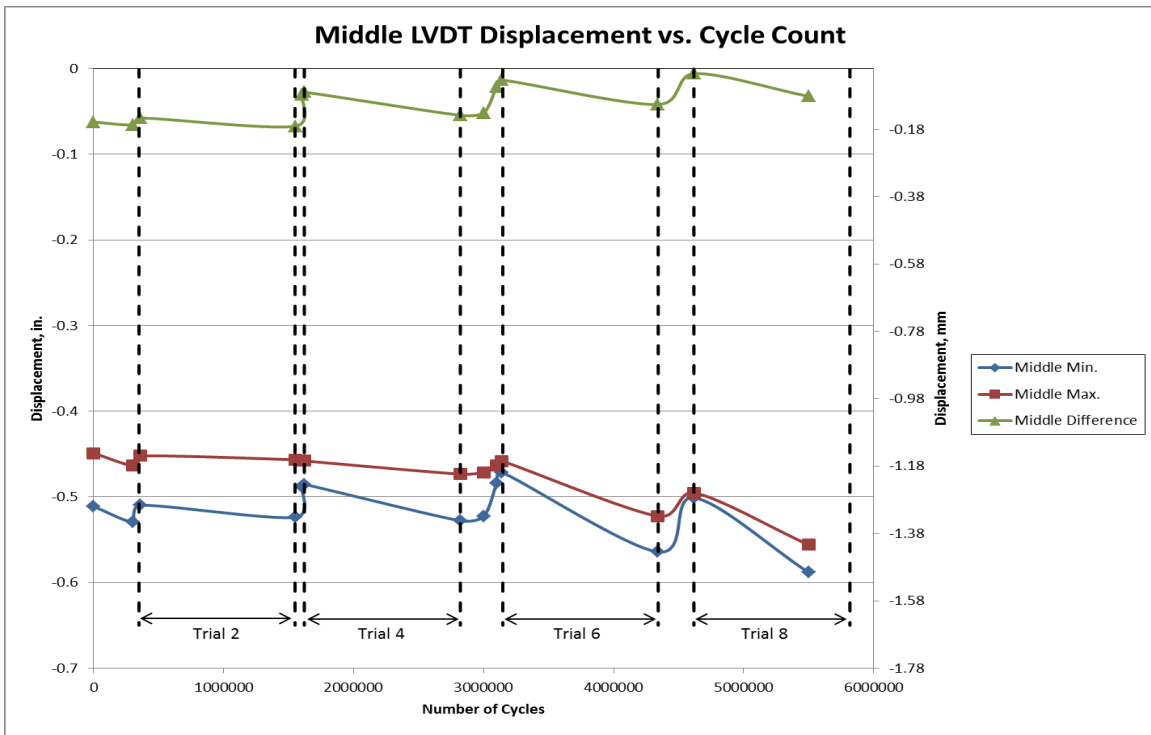


Figure 1-28: Middle LVDT displacement minima and maxima

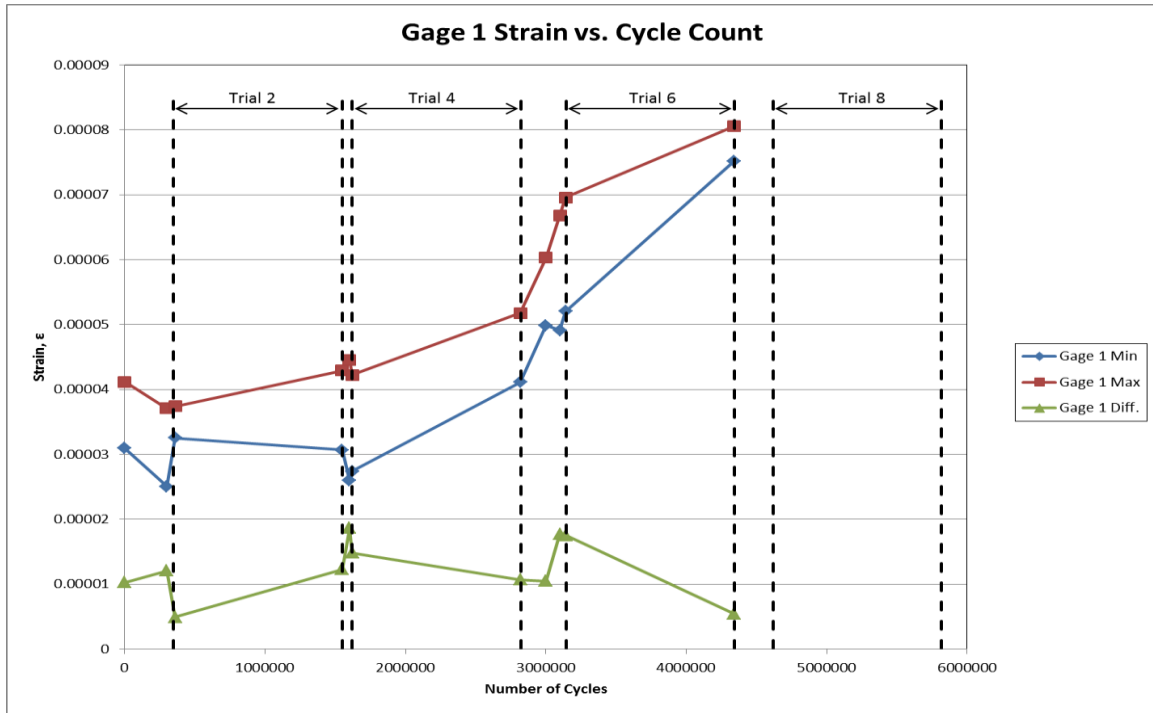


Figure 1-29: Specimen 3 strain maxima and minima

Conclusions

Research on the repair method for distortion-induced fatigue showed that the angles-with-plate repair was a very effective method to reduce the fatigue crack propagation rate in damaged beams. Computer simulations of girder subassemblies tested under fatigue loading showed that areas in the web-gap region of the model exhibiting the highest maximum principal stress demands correlated closely with the locations of fatigue cracks observed in the experiments. Both computer simulations and girder tests showed that there were two primary cracks that formed in the web-gap region: a horseshoe-shaped crack along the toe of the weld between the CP and the girder web, and a horizontal crack along the toe of the weld between the web and the flange of the girder. The performance of two different retrofit measures intended to arrest the growth of these two fatigue cracks was evaluated experimentally. The fact that there

was extensive crack growth in the top web-gap of specimen 2 and very little growth in the top web-gap of specimen 3 bears consideration. A possible reason for this difference was likely due to weld quality—it was observed that the weld in the top web-gap of specimen 3 was slightly larger than the matching weld in specimen 2. This could have caused crack growth in specimen 3 to be postponed until the flexibility and stress field of the specimen had been altered to the point that the existing crack arrested itself and no new cracks formed.

The angles-with-plate retrofit measure was effective in preventing the distortion of the web-gap region, drastically reducing the stress demands calculated at the critical points. Finite element simulations showed that stress demands at the critical points of the web-gap region reinforced with the angles-with-plate repair were on the order of 5% of those in the unreinforced configuration. The manner in which fatigue cracks propagated during experimental simulations of beam subassemblies was consistent with the results from the computer simulations. Beams in which the angle-with-plates retrofit measure was implemented experienced negligible crack growth under the same load range that caused severe fatigue damages to the web-gap region of unretrofitted specimens.

Crack-stop holes were effective in removing the sharp crack tips, preventing crack growth in the specimens by the number of cycles corresponding to fatigue crack initiation. Because crack stop holes had a negligible effect on the stress demand, and given the relatively small size of the holes evaluated, the number of cycles to crack reinitiation was comparable to the number of cycles to fatigue crack initiation in the unretrofitted configuration, and an order of magnitude lower than the number of cycles imposed on the retrofitted specimens without any measurable crack growth. The crack-stop holes seem to have little effect in situations where distortion-induced fatigue controls.

CHAPTER 2 USE OF BOLTED CFRP OVERLAYS TO PREVENT FATIGUE DAMAGE IN WELDED STEEL COVER PLATES

Abstract

Previous studies have shown that carbon fiber reinforced polymer (CFRP) overlays have been very effective to increase the fatigue life of welded cover plate connections. The effectiveness of the overlays stems from a reduction in stress demand at the welds due to a new load path through the composite material. In order for this type of retrofit measure to remain effective, the overlay must remain attached to the steel. Laboratory experiments have shown that bonding failure between the composite overlay and the steel is difficult to prevent when there are out-of-deformations.

This study is focused on exploring new approaches to prevent debonding of the composite overlays. In this new approach, bond is maintained by introducing an additional steel plate and fastening the whole assembly together with tensioned bolts. It is hypothesized that if the bolts can impart a sufficiently large compressive force on the interface between the composite material and the steel, this type of failure can be precluded.

Introduction and Background

There are many different techniques employed to prolong the life of steel bridges and other steel structures. If fatigue cracks are found during bridge inspections, engineers are compelled to implement some type of repair to prevent further crack growth. If connection details susceptible to fatigue damage are identified prior to crack initiation, a strengthening scheme may be implemented to prevent the cracks from initiating at all.

Welded connections have been shown to be particularly vulnerable to fatigue damage. Some of the methods used to prevent crack initiation rely on the introduction of residual compressive stresses into the weld toe by some form of cold-working. Shot peening, air-hammer peening, and laser shock peening are three such processes. Ultrasonic impact treatment (UIT) is another such method that generates ultrasonic impulses and ultrasonic stress waves in the material, which reduces its resistance to deformations and imparts residual compressive stresses through an accompanying impact force (Stanikov 2004). These methods reduce the effective stress at the point of distress during operation, thereby increasing fatigue life. A similar effect can be achieved by applying a composite overlay, such as CFRP, to provide an alternate load path and reduce the demand at the welded connection.

Carbon Fiber Reinforced Polymers are often arranged into layers (plies) and are made of two main components, fiber and matrix material. The plies of graphite fiber are arranged with matrix material (usually resin epoxy) and the components are cured using heat and pressure. The heat allows the matrix material to encase the fibers and the pressure works to remove any air voids. This process increases the consolidation of the composite, which is a measure of the air void volume. With lower air void volume (higher consolidation), composites have greater strength and are more resistant to crack propagation and debonding (Mallick 1993).

While CFRP overlays have been shown to increase the life of welded connections (Kaan 2012), when debonding takes place, it occurs rapidly and leads to a complete failure of the repair (Kim 2011). Research conducted by Colombi noted that the resistance of a CFRP to external and internal delaminations was a function of the shear strength of the bond material (2003). Kim notes that if the bond-slip problem could be improved, the efficacy of CFRP overlays as a retrofit measure would be greatly increased (2011). A method to improve the durability of the bond

between the composite and the steel under fatigue loading is investigated in this study. The method consists of adding tensioned bolts and a steel plate to a CFRP-resin-steel assembly (Fig. 2-1). The bolts are beneficial to improve the durability of the bond because they reduce the demand on the steel-composite interface due to force transmitted directly through them, and because the tension force in the bolts maintains the steel composite interface under compression, arresting any cracks that develop due to fatigue.

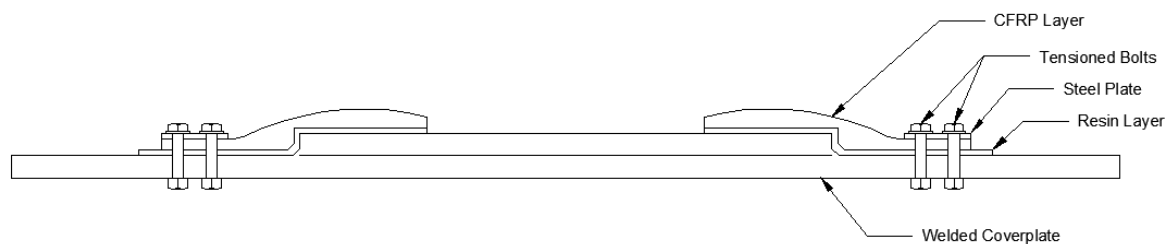


Figure 2-1: Welded cover plate with proposed bolted CFRP retrofit

Previous studies have investigated the effectiveness of adding post-tensioned bolts as a retrofit technique and using them in conjunction with UIT to prevent fatigue damage to welded connections. Villhauer (2011) found that UIT treatment resulted in better performance than a combination of bolts and UIT (at the locations indicated in Fig. 2-2). As tested, the bolts imparted tensile stresses into the transverse welds, rather than the expected compressive stresses, thus hindering the effectiveness of the retrofit measure (Villhauer 2011). For this reason, great care should be taken when choosing the location of the bolts in the proposed bolted CFRP retrofit measure so that no additional tensile stresses are induced at the weld. It should be noted that in Villhauer's tests, even though the welded cover plate specimen geometry is identical to the one used in this study, the locations of the bolts are quite different.

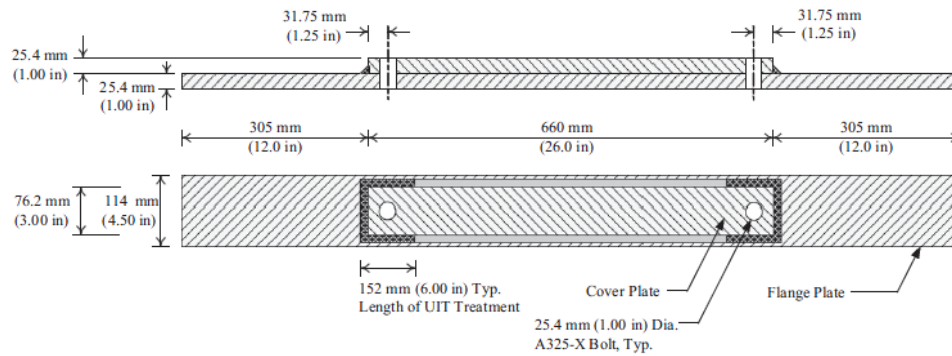


Figure 2-2: Schematic Category E' fatigue specimen (Villhauer 2011)

This retrofit measure investigated in this study is an extension of work done by Kaan (2012) and Alemdar (2012) investigating the use of CFRP overlays on welded connection plates. While the cover plate specimens used by Kaan (2012) and Alemdar (2012) are identical to the configuration used in this study, the profile of the composite overlay is significantly different to allow for the inclusion of the bolted plates. Figure 2-3 shows the loading apparatus and specimens used by Kaan (2012) with the CFRP overlays attached to the cover plate. This specimen configuration constitutes the basis of the FE models evaluated in this study, as well as a future experimental program to validate the computer simulation findings. Like other researchers (Kim 2011), Kaan (2012) found that propagation occurred quickly after debonding of the overlay was first observed. Kaan (2012) observed that debonding initiated at the edge of the overlay closest to the support and propagated towards the weld toe. Because that part of the specimen has only one plate, it is the most flexible and experiences the largest change in vertical deformations, which leads to significant peel stresses at the interface. For these reasons, this location was chosen for the placement of the bolted steel plate (Fig. 2-1).

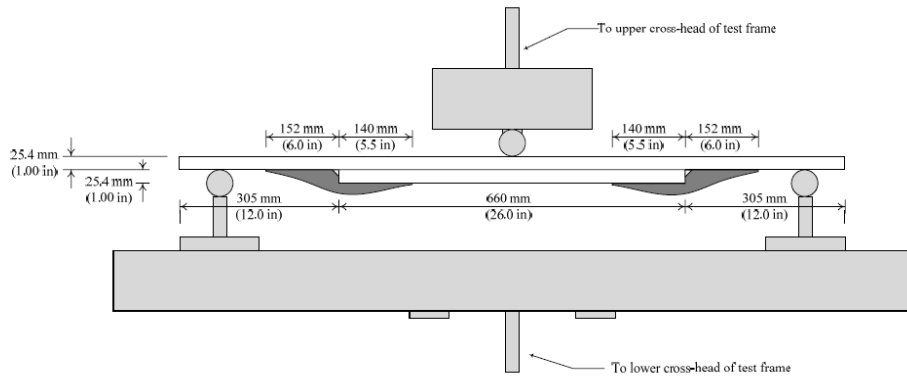


Figure 2-3: Schematic of Three-Point Bending Fixture with CFRP-Stiffened Specimen (Kaan 2012)

Objective and Scope

The main objective of this study was to investigate different configurations of CFRP overlays with bolted steel plates that can be applied to welded steel cover plate specimens. The goal of the research is to identify configurations that are potentially most effective in preventing debonding of the CFRP layer from the welded cover plate assembly. Different configurations were examined using finite element analysis to determine what levels of compressive stress could be obtained in the steel-composite interface at the location with the highest potential for debonding. Configurations with the highest compressive stress at the interface (or lowest tensile stress) were considered to be the most favorable.

Computer Simulation and Results

The computer models were created to simulate the welded cover plate specimens as closely as possible. The 8-mm ($\frac{5}{16}$ -in.) fillet welds that connect the base steel plate to the cover plate were modeled with triangular cross-sections and joined to the plates. The boundary conditions enforced on the computer models were intended to replicate the support and loading conditions used in the three-point bending specimens. In order to reduce computation time,

advantage was taken of symmetry and only half of the actual specimen was modeled. The center of the specimen was restrained against rotation and translation, and the free end of the specimen had no constraints. The centerline labeled in Fig. 2-1 indicates where this boundary position replaced the other half of the model (located at the left end of Fig. 2-2).

A pressure load of 16.5 MPa (2.4 ksi) was applied over a 6.4-mm ($\frac{1}{4}$ -in.) long strip of the full 114-mm ($4\frac{1}{2}$ -in.) width of the base steel plate. The dimensions of this load area correspond to the three-point bending test apparatus and the loading provides a stress of 172 MPa (25 ksi) in the extreme tension fiber of the cover plate. When bolts were included in the model, they were 13-mm ($\frac{1}{2}$ -in.) diameter bolts with the same material properties as the other steel components. All configurations were modeled using linear elastic material behavior. The steel properties were defined as follows: a Young's Modulus of 192 GPa (27,800 ksi) and a Poisson's ratio of 0.3. The resin was given the following properties: a Young's Modulus of 2.1 GPa (300 ksi) and a Poisson's ratio of 0.15. Finally, the CFRP was given the following properties: a Young's Modulus of 13.8 GPa (2000 ksi) and a Poisson's ratio of 0.1.

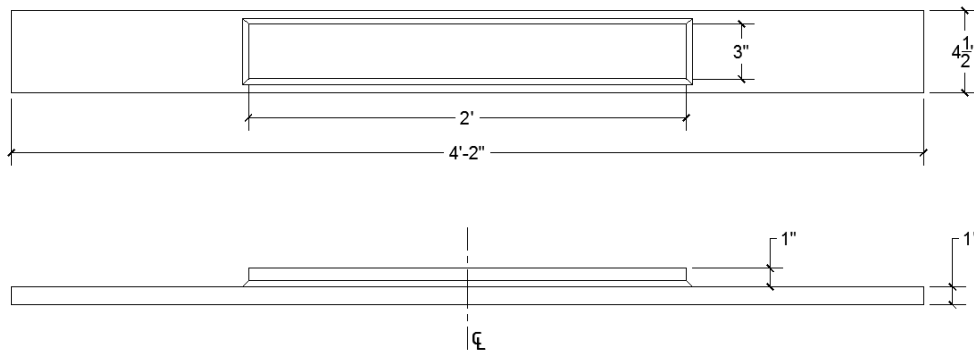


Figure 2-4: Welded cover plate plan and elevation

A base model with a rectilinear overlay attached to the ends of the steel cover plate (Fig. 2-5) was used as the basis of comparison for the various configurations evaluated. A steel plate 102-mm (4-in.) long by 76-mm (3-in.) wide with the same material properties as the cover plate was placed on top of the overlay and attached to the cover plate with two bolts spaced at 51-mm (2-in.). A bolt load of 53-kN (12-kip) was defined for each bolt following the specifications in AISC Steel Construction Manual (AISC 16.1-103) for the minimum allowable bolt tension in slip-critical connections. A resin layer 6-mm ($\frac{1}{4}$ -in.) thick was modeled between the cover plate and the composite overlay and connected to both using tie constraints. This layer was flush with the composite overlay except at the free end of the specimen, where the resin extended beyond the overlay a length of 6-mm ($\frac{1}{4}$ -in.), creating a pool of resin that was only bonded to the steel. The purpose of this resin pool was to decrease the chance of debonding by reducing the stress concentration at the change in thickness of the different materials (Kaan 2012).

The computed stress values were taken at the composite-resin interface and the resin-steel interface at the free end of the specimen. The highest stresses along the two interfaces of the rectilinear CFRP configuration were used as the reference values to compare with the other configurations. A summary of the results is presented in Table 2-1. The rectilinear overlay configuration (Fig. 2-2) is less desirable because it uses a larger quantity of material and would require more effort to fabricate—both factors would increase the cost of the retrofit measure. The principal stress orthogonal to the contact plane between the base steel plate and the cover plate was used as a gauge of the effectiveness of the retrofit measure because it is an indicator of the magnitude of the peel stress, which has been shown to be very detrimental to the bond between the steel and the overlay (Alemdar 2012). This stress component is referred to in this study as the S33 stress direction. In an ideal configuration, the compressive stress in the S33

direction would be maximized and the tensile stress would be minimized throughout the interfaces of the steel, resin, and composite layers. The S33 stress values for the rectilinear overlay configuration were -13.8 MPa (-2 ksi) at the composite-resin interface and 10.3 MPa (1.5 ksi) at the resin-steel interface.

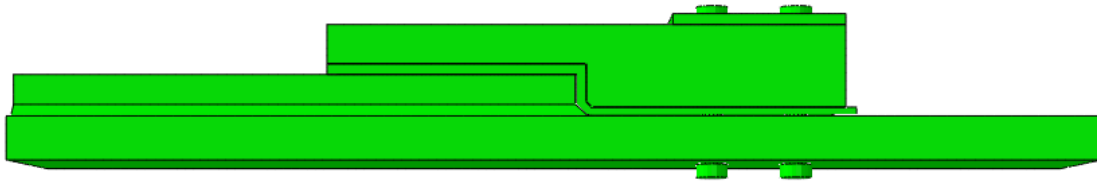


Figure 2-5: Rectilinear overlay model

In the studies by Kaan and Alemdar, the overlays were fabricated with a curved profile with the intent of reducing the stress demand at the interface, near the edges of the overlay (Fig. 2-3). A section cut of the curved overlay configuration showing the S33 principal stress is shown in Fig. 2-7. The computed stress at the composite-resin interface was found to be -11.7 MPa (-1.7 ksi) and the stress at the resin-steel interface was found to be 4.8 MPa (0.7 ksi) (Table 2-1). While the compressive stress at the composite-resin interface was found to be slightly lower than the rectilinear overlay configuration, the tensile stress at the resin-steel interface had a sizeable reduction.

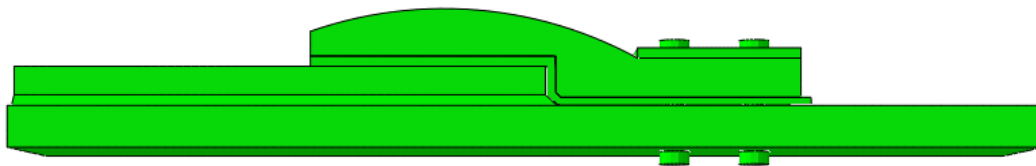


Figure 2-6: Curved overlay model

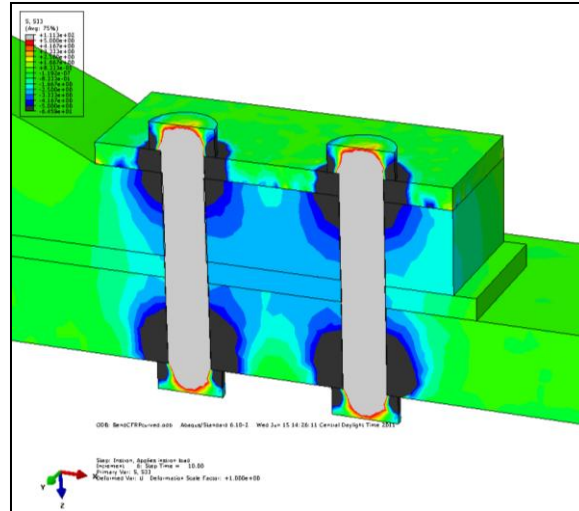


Figure 2-7: Section cut of curved overlay showing S33 stresses

The next configuration that was analyzed had a thinner overlay (Fig. 2-8). The CFRP overlay was reduced to 13-mm ($1/2$ -in.) so the compressive stress induced by the steel plate would be closer to the steel-resin interface. All other aspects of the model were identical to those of the curved overlay configuration. The computed S33 stresses in the composite-resin and resin-steel interfaces were -30.3 MPa (-4.4 ksi) and 4.8 MPa (0.7 ksi), respectively (Table 2-1). As intended, this configuration achieved a much higher compressive stress at the interface than the rectilinear overlay, and also reduced the tensile stress at the resin-steel interface. A thinner overlay was not analyzed due to concerns about placing a very high stress demand on the composite material.

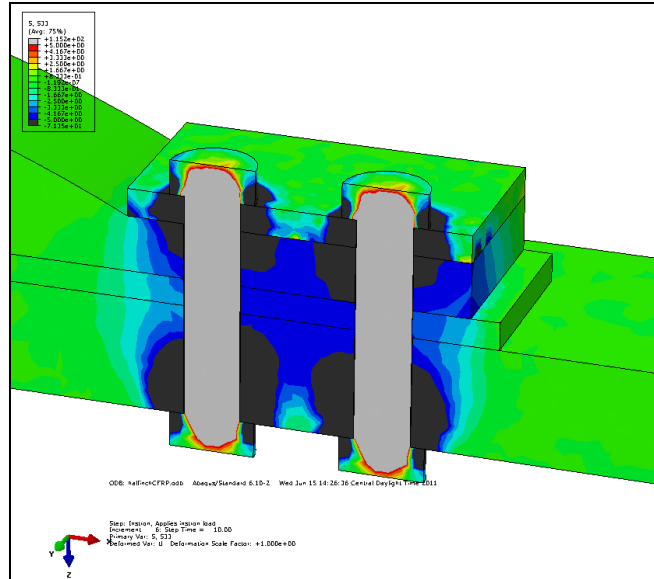


Figure 2-8: Section cut of 1/2-in. overlay showing S33 stresses

Another parameter that was analyzed was the spacing between the two bolts used to attach the overlay. The gage length and edge distance were taken as the minimum allowable values as allowed in the AISC specification (AISC 16.1-106/107). The bolt spacing was reduced to 38-mm (1-1/2-in.) and the edge distance was reduced to 19-mm (3/4-in.). The length of the steel plate was reduced to 76-mm (3-in.) to accommodate the change in the spacing. All other model and material properties were kept the same as the curved overlay model. Results showed that the calculated stress was -26.9 MPa (-3.9 ksi) in the composite-resin interface and 4.1 MPa (0.6 ksi) in the resin-steel interface (Fig. 2-2). The effect of reducing the bolt spacing was a significant increase in compressive stress and a decrease in tensile stress.

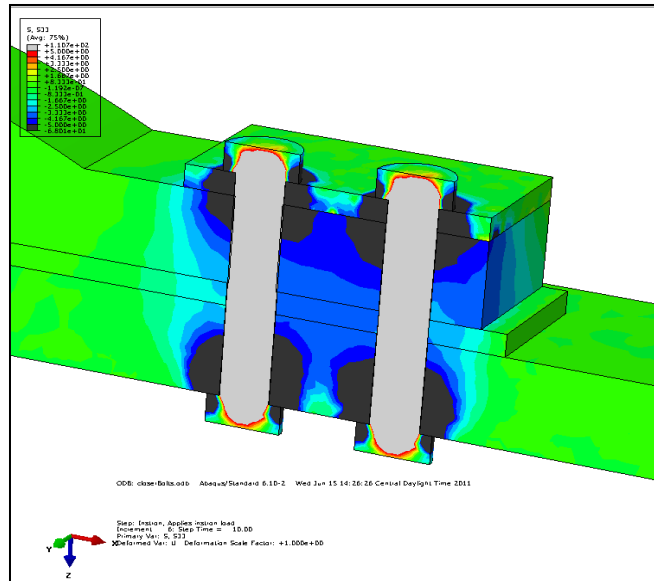


Figure 2-9: Section cut of overlay with closer bolt spacing showing S33 stresses

Two more parameters were analyzed to investigate other alternatives to reduce the tensile stress demand at the resin-steel interface. The effect of increasing the length of the resin pool (the length of resin that extended beyond the overlay) was investigated by analyzing models without a resin pool and with a 25-mm (1-in.) resin pool. The curved overlay model was used with the only variation being the length of the resin pool. The model without a resin pool, had computed stresses in the composite-resin and resin-steel interfaces of -11.7 MPa (-1.7 ksi) and 4.1 MPa (0.6 ksi), respectively (Fig. 2-7). The model with a 25-mm (1-in.) resin pool had computed stresses of -11.7 MPa (-1.7 ksi) and 0.5 MPa (0.07 ksi), respectively (Fig. 2-8). As was expected, the presence of the resin pool had a negligible effect on the stress in the composite-resin interface. However, the model with the 25-mm (1-in.) resin pool showed a significant decrease in the tensile stress demand at the resin-steel interface.

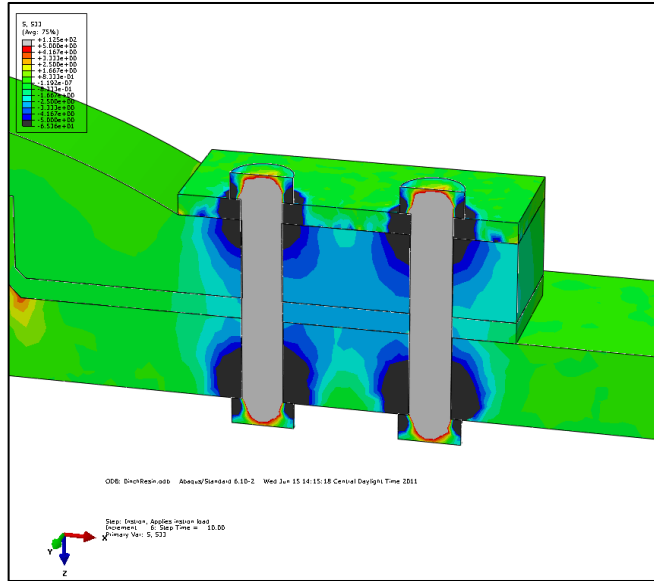


Figure 2-10: Section cut of specimen without a resin pool showing S33 stresses

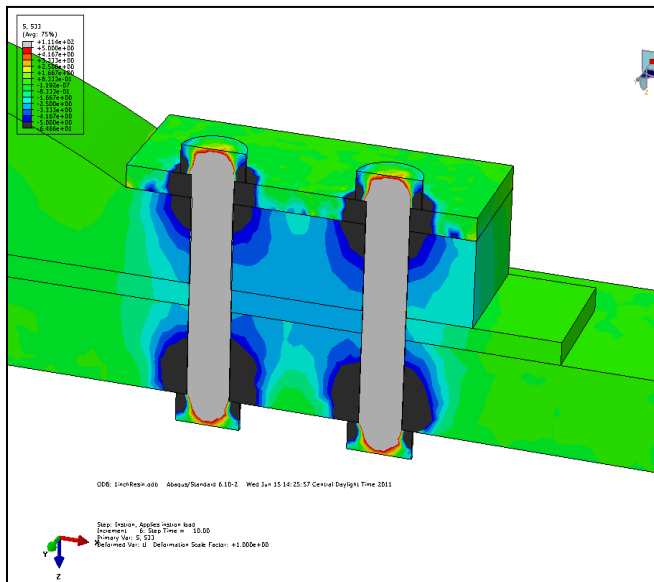


Figure 2-11: Section cut of specimen with 1-in. resin pool showing S33 stresses

Table 2-1: Stresses at composite-resin/resin-steel interfaces for configurations analyzed

Configuration	Composite, MPa (ksi)	Resin, MPa (ksi)
Rectilinear overlay	-13.8 (-2)	10.3 (1.5)
Curved overlay	-11.7 (-1.7)	4.8 (0.7)
½-in. overlay	-30.3 (-4.4)	4.8 (0.7)
Closer bolt spacing	-26.9 (-3.9)	4.1 (0.6)
No resin pool	-11.7 (-1.7)	4.1 (0.6)
1-in. resin pool	-11.7 (-1.7)	0.5 (0.07)

Conclusions

Research on composite overlay retrofit measures using computer simulations showed that the principal S33 stresses at the edge of the composite-resin and resin-steel interfaces could vary significantly by changing the dimensions of the retrofit measure. Changes in the thickness of the overlay had a significant effect on the stress demand at the composite-resin and resin-steel interfaces. Configurations with thinner overlays were more favorable because they showed the largest compressive stresses at the interface layer. Reducing the bolt spacing achieved a similar result. The proximity of the bolts led to higher compressive stresses over a shorter region of the overlay. A resin pool of 25-mm (1-in.), extending from the edge of the composite, led to a significant reduction in the tensile stress at the edge of the resin-steel interface.

Based on the simulations that were performed, it is concluded that the most effective retrofit measure would employ a thinner overlay 13-mm (¹/₂-in.) thick, with two bolts spaced at 38-mm (1-¹/₂-in.), and a 25-mm (1-in.) long resin pool.

CHAPTER 3 LOAD CELL DESIGN FOR SCALE BRIDGE MODEL

Abstract

When testing reduced-scale bridge systems for distortion-induced fatigue, load distribution is an important factor because it might provide indications of damage to connections between the girder webs and the cross-frames. In order to monitor the load distribution in a 30-ft reduced-scale bridge model used to investigate retrofit measures for distortion-induced fatigue, high-capacity load cells were required. Because commercially-available fatigue-rated load cells are quite expensive, six low-profile pancake-style load cells were designed, fabricated, instrumented, and calibrated to be used in the test. A low profile configuration was selected to meet clearance constraints imposed by the reaction frame. This configuration was analyzed using a finite element model to proportion the load-cell so that stress demands would remain within acceptable thresholds, and to identify locations for optimal placement of strain gages. In order to get the most use out of the load cells, they were designed to be used in tension, as well as compression, and to be reconfigurable.

Introduction

Load cells were needed to monitor load distribution in a 30-foot reduced-scale bridge model designed to test retrofit measures for distortion-induced fatigue damage. The bridge model had three girders and six supports (Fig. 3-1). As cracks form during the testing of the bridge specimen, the stiffness of the assembly changes. Because differential deflection is the driving effect that causes distortion-induced fatigue damage, it is important to monitor and correlate load distribution to girder deformation. For this reason, an important aspect of the

research program was to quantify the change in load distribution throughout the three girders and the six supports of the bridge model.

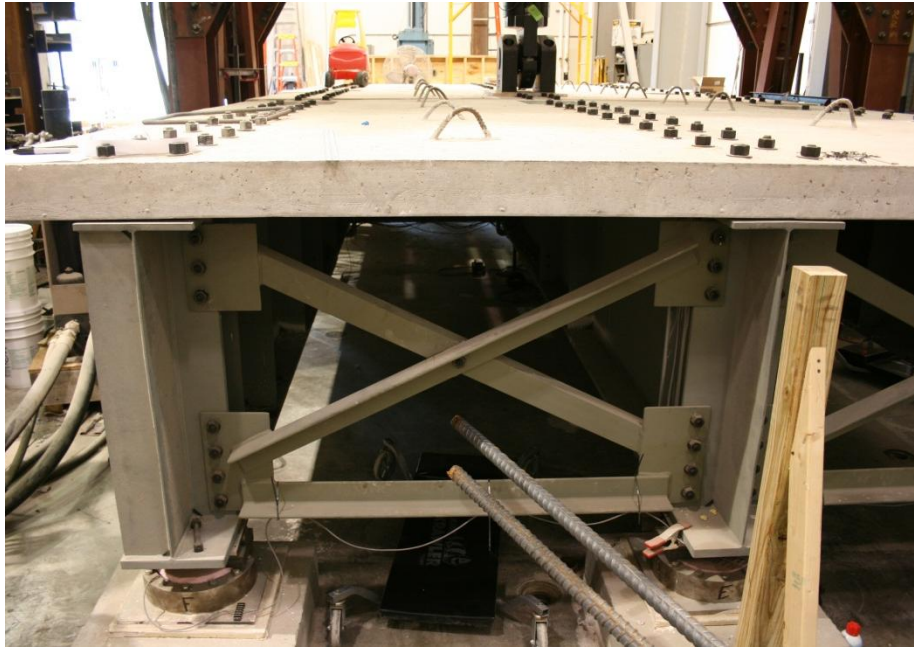


Figure 3-1: View of end of bridge setup with load cells in place

Given the extremely high cost of commercially-available fatigue-rated load cells, and the high cost of repair in case of damage, it was decided that load cells fabricated in house would be considerably cheaper, easier to repair, and provide the option of customizing the length to meet the available clearance constraints.

Objective and Scope

The objective of this paper is to describe the design and fabrication of six load cells that could be used to monitor load distribution in a 30-foot reduced-scale bridge model. The process consisted of choosing a general configuration and analyzing it using a finite element model. The original configuration was altered based on the analysis results to achieve the optimum stress levels at the positions where strain gages would be located. Also taken into account were load

capability, weight of the apparatus, and serviceability (when applying strain gages and wiring). After the design was finalized, fabrication drawings were produced and provided to a qualified machine shop. After fabrication, the load cells were instrumented with strain gages in a full Wheatstone bridge configuration and subsequently calibrated.

Load Cell Design

For several reasons, pancake-style load cells were chosen for this application. This particular configuration has a low-profile, can be easily sealed from the environment, and is very insensitive to off-axis loading. These cells rely on measuring shear strain (requiring the gages to be attached at 45 degree angles with respect to the vertical load axis). Dual gages were used to improve the sensitivity of the load cells.

The basic configuration had a diameter of 330-mm (13-in.) with eight cutouts with diameters of 51-mm (2-in.). Each pair of cutouts was joined by the removal of the material in between (Fig. 3-3). These interior cutouts essentially created four web portions of material that connected the interior of the load cell to the exterior. There was a raised ridge around the perimeter of the cells that provided the support, such that when load was applied, the four connecting webs experienced most of the deformation and stress demand (Fig. 3-6). Figure 3-2 shows the load cells in use at a girder end of the reduced-scale bridge model.



Figure 3-2: Load cell at girder support

A base was also included in the drawings in Fig. 3-4a, and it is connected to the load cell with twelve structural bolts. Additionally, both the load cell and the base have 25-mm (1-in.) diameter threaded holes in their centers so that two threaded rods can be inserted at each end for the purpose of tension testing. However, the base is designed to be used in both tension and compression testing, as it provides a level support for the load cell. Figure 3-4b shows the compression component which is attached during compressive load testing. This piece transfers the applied load to the inner core of the load cell. It was designed as a separate piece to avoid additional reentrant corners in the load cell, which would create areas of high stress demand, and the fact that it is a separate piece makes fabrication much easier. Finally, a schematic of the completed assembly is shown in Fig. 3-4c in the configuration that will be used in the scale bridge test.

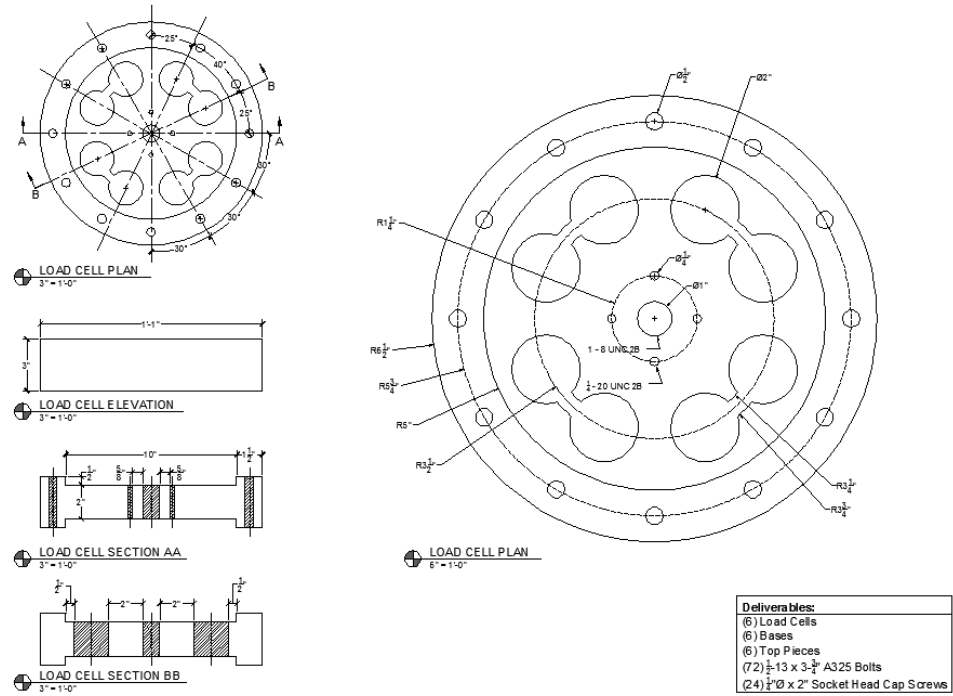


Figure 3-3: Load cell schematic

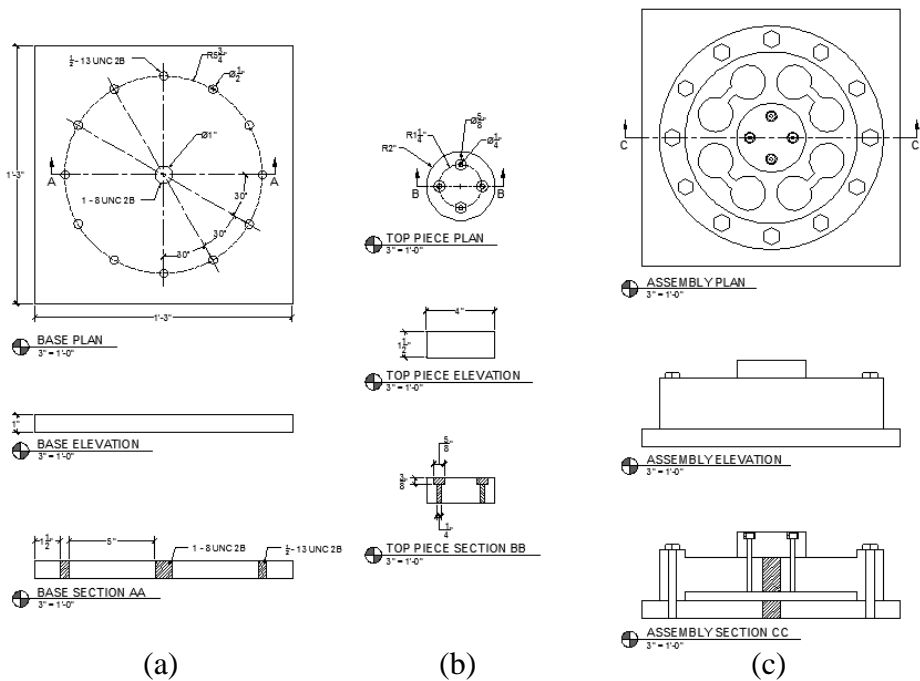


Figure 3-4: Load cell schematics: a) tension base b) compression piece c) assembly

Computer Simulation

A finite element analysis was conducted using the configuration shown in Figs. 3-3 and 3-4. The three parts (base, load cell, and the top piece) were modeled individually and built into an assembly. The three components were connected using tie constraints (Fig. 3-5), because the effects of the bolts, or the interaction between the components were not considered to be significant. The tension base was fixed in place and restrained against rotation and translation. All three parts were defined with the following steel properties: a Young's Modulus of 200 GPa (29,000 ksi) and a Poisson's ratio of 0.3. A 222-kN (50-kip) force was applied to the top of the compression piece and the resulting stress field was calculated.

Figure 3-6 shows the von Mises stresses on the load cell alone; the maximum stress at the center of the connecting web portions (the interior surface of the 51-mm, 2-in. diameter cutouts) was computed to be 90 MPa (13 ksi). The maximum principal stress at this location was computed to be approximately 45 MPa (6.5 ksi). Additionally, the maximum principal strain at this point was found to be 310 $\mu\epsilon$. These stress and strain values are important for determining the load capacity of the cells and the kind of strain gages best suited for the expected strain range. Near the point of application of the 222-kN (50-kip) load, the maximum von Mises stress in the models was 124 MPa (18 ksi). Based on the yield strength of the steel used, a ratio of load to stress can be used to determine the maximum allowable load. Additionally, because the maximum principal strain for the gages selected was on the order of 1000 to 1200 $\mu\epsilon$, fatigue on the strain gages is not expected to be a significant problem (Vishay 2012).

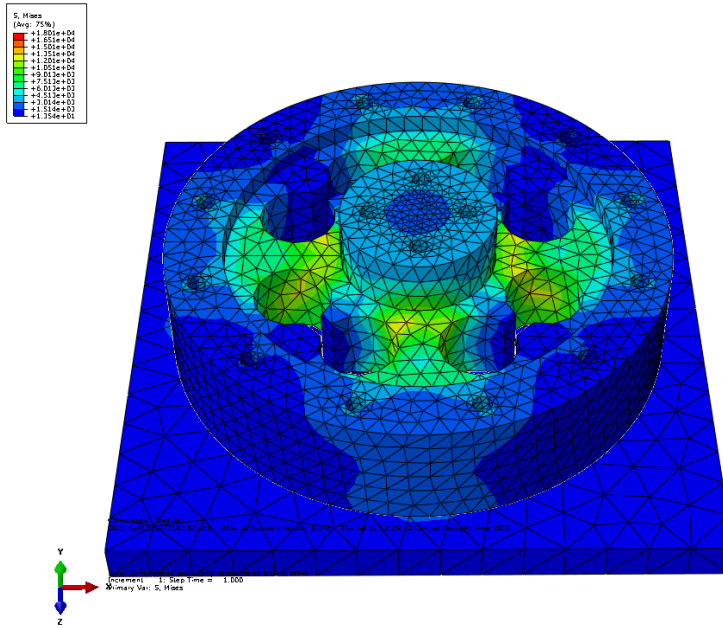


Figure 3-5: Computed stresses in load cell assembly

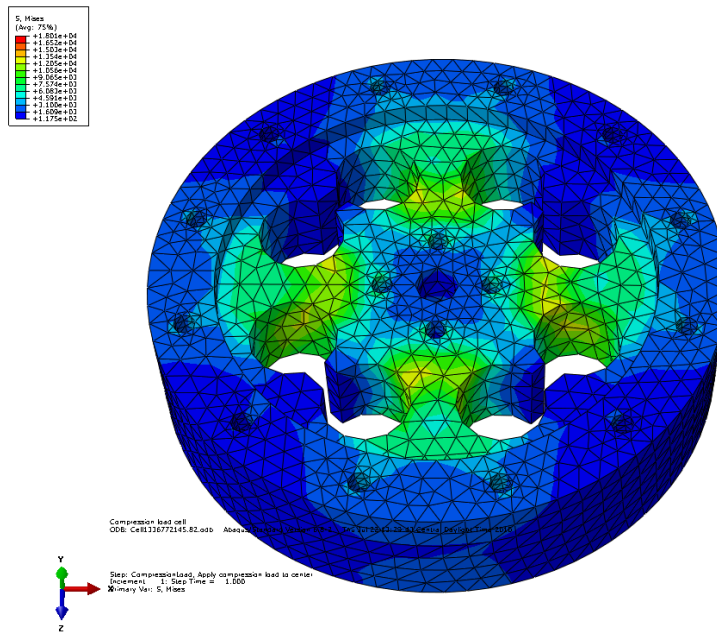


Figure 3-6: Computed stresses in load cell alone

Fabrication, Instrumentation, and Calibration

The shop drawings sent out for fabrication are shown in Figs. 3-3 and 3-4. The fabricator provided steel with a yield strength of 930 MPa (135 ksi); there was no heat-treating or plating, and the surfaces were machine finished. Figure 3-7 shows the load cell assemblies in the condition that they were received from the fabricator.

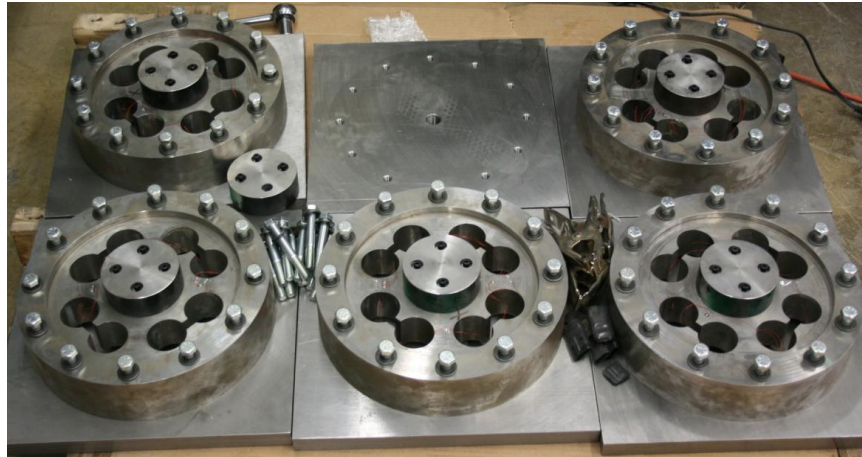


Figure 3-7: Fabricated load cells

The strain gages selected for the load cells were dual-grid transducer-class shear gages, model number J2A-06-S036X-350, provided by Vishay Precision (Fig. 3-8). As previously mentioned, the dual-grid gages allow for higher precision measurements, and the gages are already oriented at 45 degrees with respect to the horizontal and vertical axis. The surface of the load cells was prepared following the recommendations of the manufacturer (Vishay 2012) for the application of the strain gages, and they were adhered using M-Bond 600 (also provided by Vishay), which is used for high-performance applications, such as long-term fatigue testing. The M-Bond 600 required a curing temperature above operating temperature of at least 30° C (50° F). After the strain gages were attached to the surface of the load cells, the gages were clamped in place using a square of silicone, pieces of wooden cylinders cut in half through the axis, and

metal spring clamps. The epoxy was cured in an oven at 150° C (300° F) for at least 2 hours. The silicone was used to provide a uniform distribution of clamping pressure, and the wooden pieces served as intermediary load distribution between the clamps and the silicone.

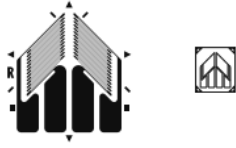
GAGE PATTERN		Actual size shown. Enlarged when necessary for definition.		GAGE DESIGNATION See Note 1	RES. IN OHMS	STANDARD CREEP CODE	ENCAPSULATION OPTION AVAILABLE
DIMENSIONS		inch	millimeter				
				Encapsulated version of T031/T032.			
GAGE LENGTH	OVERALL LENGTH	GRID WIDTH	OVERALL WIDTH	J2A-XX-S036R-350 J5K-XX-S1448-350/DP			
0.075	0.22	0.060	0.190				
1.91	5.6	1.52	4.83				
MATRIX SIZE	0.28 L x 0.25 W		7.1 L x 6.4 W		350 ± 0.4%	R	N/A
				350 ± 0.4%			

Figure 3-8: Strain gage diagram (Vishay 2012)

After cooling, the load cells were wired in a full Wheatstone bridge configuration (Fig. 3-9). Figure 3-10 shows a strain gage in place after being wired. The conductor used in the wiring was single-strand copper wire with a polyurethane enamel coating. The enamel was removed by applying heat from a soldering iron where it was necessary for connection. Four gages were attached to each of the four web portions of the load cells and wired as described (Fig. 3-11).

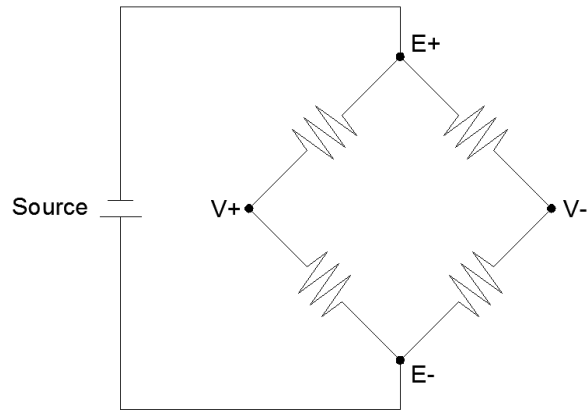


Figure 3-9: Load cell wiring diagram

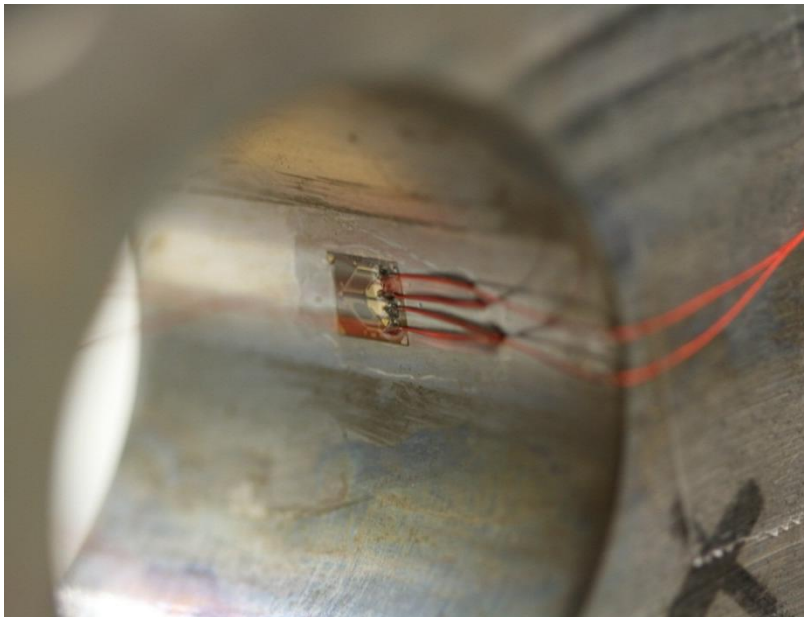


Figure 3-10: Dual-grid gage after wiring

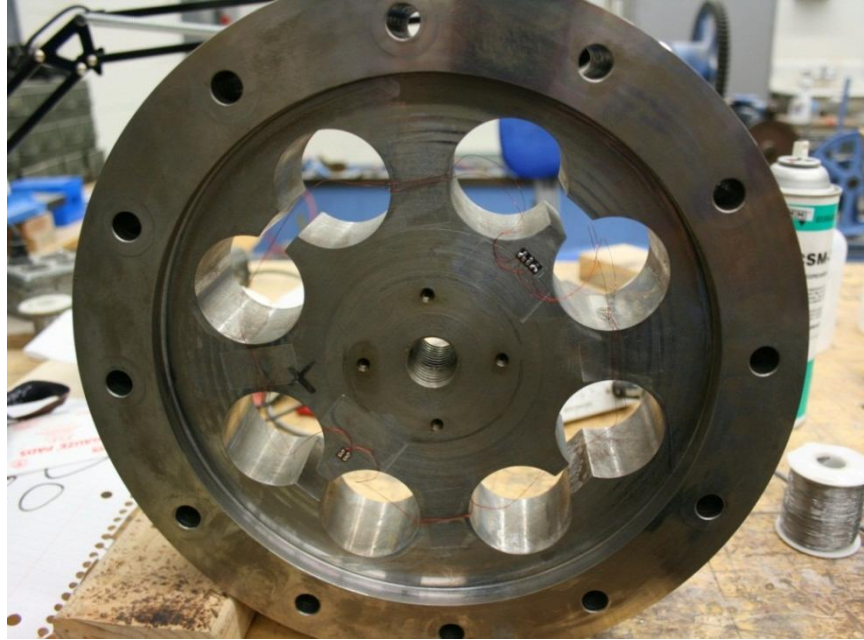


Figure 3-11: Load cell after gaging and wiring

The final step in preparing the load cells for testing was to calibrate them. A Baldwin universal test frame, periodically calibrated using NIST-traceable standards, was used for calibration of the load cells. The load cell assemblies were loaded in compression from 0 to 267-kN (0 to 60-kip); the corresponding output voltage was recorded. The plotted data for Load Cell B is shown in Figure 3-12, and the slope and intercept are calculated therein. This calibration was carried out for all six load cells, labeled A through F and will be used for data collection in the scale bridge test. The curve in Fig. 3-12 shows the high linearity of the relationship between the output voltage and the load, and the coefficient of correlation r^2 of approximately 1.0 shows that the load cell configuration was very effective.

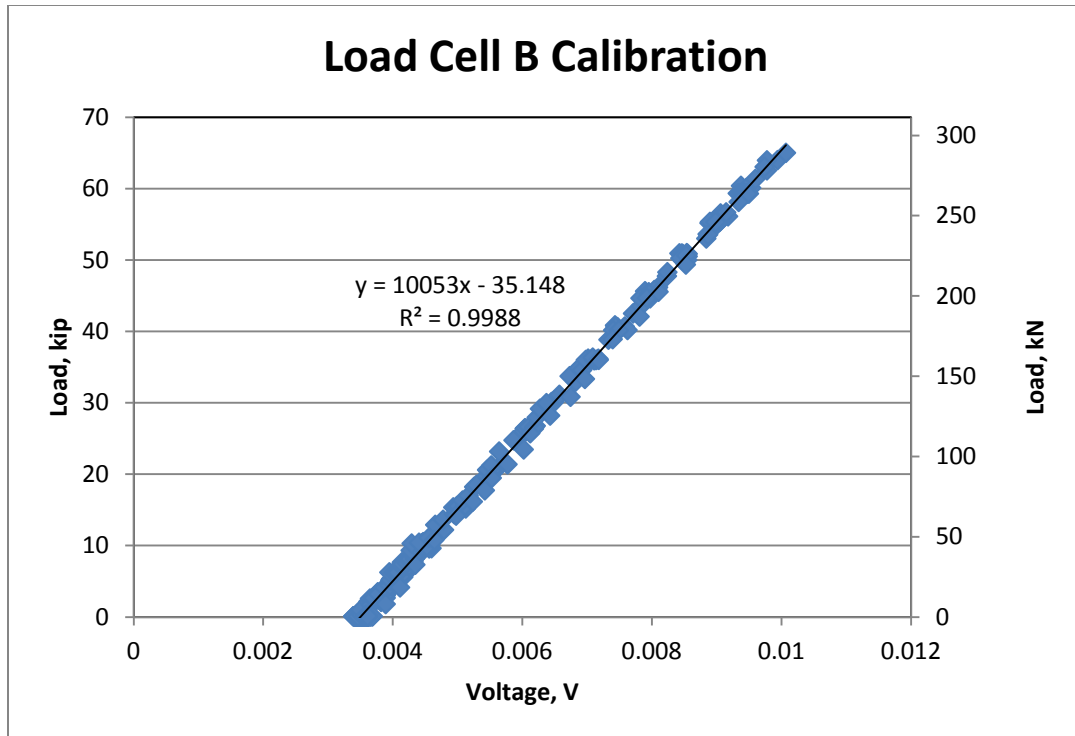


Figure 3-12: Load cell calibration plot

Summary and Conclusions

- Research showed that load cells could be proportioned and fabricated at a significantly lower cost than commercially-available fatigue-rated load cells.
- A pancake-style configuration was adopted to be able to meet clearance constraints presented by the reaction frame. The load cell configuration was analyzed using a 3-D FE model. Under a 222-kN (50-kip) load, the von Mises stress at the location where the gages were attached was 90 MPa (13 ksi).

- The maximum principal strain at the strain gage location was $310 \mu\epsilon$, which allowed for the use of dual-grid transducer-class strain gages that were bonded using an adhesive with longevity for high-cycle fatigue testing.
- Each load cell was wired into a full Wheatstone bridge configuration and calibrated, providing a means for collecting data on load distribution in a three-girder reduced-scale bridge model.

References

- AASHTO, (2007). "AASHTO LRFD Bridge Design Specifications (2007)." American Association of State Highway and Transportation Officials.
- ABAQUS (2009) Simulia, Version 6.8-2. <http://www.simulia.com>.
- AISC (2005) "Steel Construction Manual, Thirteenth Edition." *American Institute of Steel Construction, Inc.* Chicago, IL.
- Alemdar, F., A. Matamoros, C. Bennett, R. Barrett Gonzalez, and S.T. Rolfe (2011). "Use of CFRP Overlays to Strengthen Welded Connections under Fatigue Loading." *Journal of Bridge Engineering* 1:191.
- Alemdar, F., A. Matamoros, C. Bennett, R. Barrett Gonzalez, and S.T. Rolfe (2012). "Use of CFRP Overlays to Strengthen Welded Connections under Fatigue Loading." *Journal of Bridge Engineering* Vol. 17, Issue 3
- ASTM E8/E8M (2009). "Standard Test Methods for Tension Testing of Metallic Materials."
- Castiglioni, CA, JW Fisher, and BT Yen (1988). "Evaluation of fatigue cracking at cross diaphragms of a multigirder steel bridge." *Journal of Constructional Steel Research* 9 (2):95-110.
- Colombi, P., Bassetti, A., and Nussbaumer, A. (2003) "Crack Growth Induced Delamination on Steel Members Reinforced by Prestressed Composite Patch." *Fatigue Fract. Engng. Mater. Struct.*, 26, 429-437.
- Cousins, TE, and JM Stallings (1998). "Laboratory Tests of Bolted Diaphragm-Girder Connections." *Journal of Bridge Engineering* 3:56.
- Fisher, JW (1990). "Distortion-induced fatigue cracking in steel bridges." Transportation Research Board.
- Hassel, H.L. (2011). "An Analytical Evaluation of Distortion-Induced Fatigue in Steel Bridges."
- Jajich, D, and AE Schultz (2003). "Measurement and Analysis of Distortion-Induced Fatigue in Multigirder Steel Bridges." *Journal of Bridge Engineering* 8:84.
- Kaan, B. (2012) "Fatigue Enhancement of Category E' Details in Steel Bridge Girders Using CFRP Materials." *Journal of Composites for Construction*. Vol. 16, Issue 2.

- Keating, P.B. (1994). "Focusing on fatigue." *Civil Engineering—ASCE* 64 (11):54-57.
- Keating, PB, and JW Fisher (1987). "Fatigue behavior of variable loaded bridge details near the fatigue limit." *Transportation Research Record* (1118).
- Kim, Y.J. (2011) "Interaction Between CFRP-Repair and Initial Damage of Wide-Flange Steel Beams Subjected to Three-Point Bending." *Composite Structures*. Vol. 93, Issue 8, 1986-1996.
- Lindberg, A., and A. Schultz (2007). "Incorporation of Fatigue Detail Classification of Steel Bridges into the Minnesota Department of Transportation Database."
- Mallick, P.K. (1993) *Fiber-Reinforced Composites: Materials, Manufacture, and Design*, 2nd Ed., Marcel Dekker, New York, NY.
- Roddis, K, and Y Zhao (2001). "Out-of-plane fatigue cracking in welded steel bridges." *Welding Innovations* 27 (2):2-7.
- Stanikov, E. (2004) "Physics and Mechanisms of Ultrasonic Impact Treatment." *IIW Document XIII-2004-04*, International Institute of Welding. Paris, France.
- Villhauer, B., C.R. Bennett, A.B. Matamoros, and S.T. Rolfe (2011) "Fatigue Behavior of Welded Coverplates Treated with Ultrasonic Impact Treatment and Bolting." *Engineering Structures* 34, 163-172.
- Vishay Precision Group (2012) Micro-Measurements.
<http://www.vishaypg.com/docs/11558/sheardus.pdf>